

The dynamics of western North America: stress magnitudes and the relative role of gravitational potential energy, plate interaction at the boundary and basal tractions

Lucy M. Flesch,^{1,2} William E. Holt,³ A. John Haines,⁴ Lianxing Wen³ and Bingming Shen-Tu⁵

¹Department of Earth and Atmospheric Sciences, Purdue University, 550 Stadium Mall Drive, West Lafayette, IN 47907-2051, USA.
E-mail: lmflesch@purdue.edu

²Department of Terrestrial Magnetism, Carnegie Institution of Washington, 5241 Broad Branch Road, N.W., Washington DC 20015, USA

³Department of Geosciences, State University of New York - Stony Brook, Stony Brook, NY 11794-2100, USA

⁴Department of Earth Sciences, University of Cambridge, Cambridge CB2 3EQ, UK

⁵AIR-Worldwide Corp., 101 Huntington Ave., 22nd Fl., Boston, MA 02199, USA

Accepted 2006 October 24. Received 2006 October 23; in original form 2006 February 6

SUMMARY

We investigate the forces involved in driving long-term large-scale continental deformation in western North America, and quantify the vertically averaged deviatoric stress field arising from internal buoyancy forces and the accommodation of relative plate motions. In addition, we investigate the ability of regional models to resolve the level of tractions acting at the base of the lithosphere. We directly solve force-balance equations for vertically averaged deviatoric stresses associated with differences in values of $1/(\text{lithospheric thickness})$ times the gravitational potential energy per unit area (GPE). The GPE values are inferred using both the ETOPO5 topographic data set and the CRUST2.0 crustal thickness model. Deviatoric stresses associated with basal tractions are calculated globally, with inputs determined from an isoviscous upper mantle ($\eta = 10^{21}$ Pa s) 3-D large-scale convection model in which mantle density variations were inferred from tomographic data and the history of subduction. In a 211-parameter iterative inversion we then solve for a stress field boundary condition by fitting stress field indicators (i.e. the directions and relative magnitudes of the principal axes of kinematic strain rates). Magnitudes of the total vertically averaged deviatoric stress field (sum of GPE solution with the boundary condition solution) range from 5 to 10 MPa within a 100-km thick lithosphere. These magnitudes are calibrated by the GPE differences, along with the spatial variation in deformation style. There is a trade-off between the scaling of the basal traction deviatoric stress field and the boundary condition solution. However, the combined boundary conditions plus basal traction solution is robust (in both magnitude and style), and when added to the contribution from GPE differences provides a global minimum of misfit between the total deviatoric stress solution and the stress field indicators. GPE variations account for ~ 50 per cent of the deviatoric stress magnitudes driving deformation, while boundary condition stresses account for the remaining ~ 50 per cent of deviatoric stress magnitude. By comparing possible end-member strength profiles with our vertically averaged deviatoric stresses we infer that the bulk of the strength within the lithosphere in western North America lies within the brittle seismogenic layer.

Key words: basal tractions, continental deformation, driving forces, mantle convection, stress distribution, western North America.

1 INTRODUCTION

The plate boundary zone through western North America is broad and spatially complex. The recent accumulation of space based geodetic data has dramatically improved our understanding of crustal relative motions, strain rates, and how strain is accommodated across this broad zone of diffuse continental deformation (Dixon *et al.* 1996; Shen-Tu *et al.* 1998, 1999; Bennett *et al.* 1999, 2003; Kreemer *et al.* 2003; Thatcher 2003; Hammond & Thatcher 2005). Although the deformation gradients within the plate boundary zone vary spatially from nearly zero-level

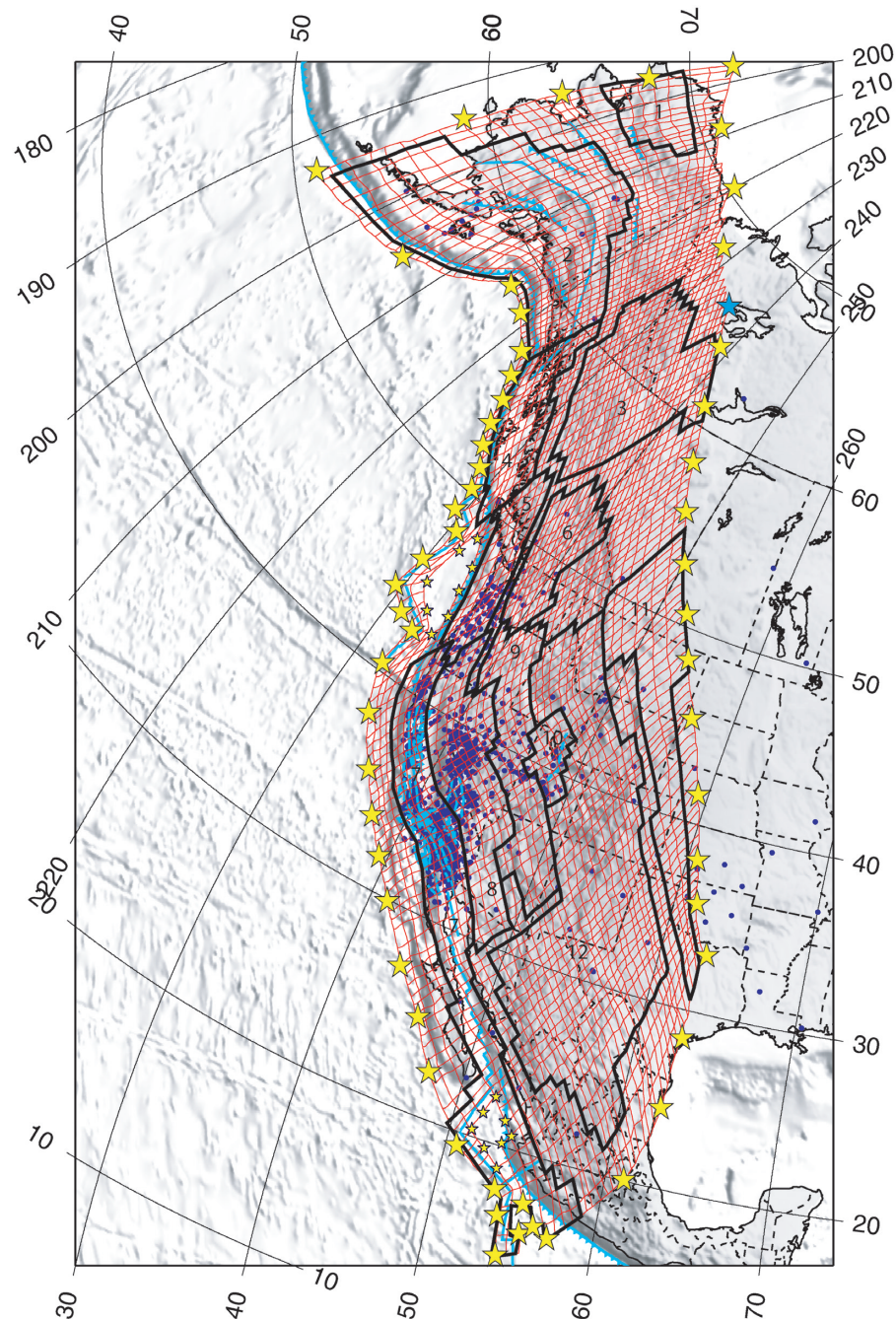


Figure 1. The grid (red region) used in the kinematic and dynamic modelling. We have defined rigid regions to simulate the Pacific, Rivera, Cocos, Juan de Fuca and North American Plates. Blue dots represent the GPS and VLBI data (see references in main text) used in this study, quaternary fault slip rate data (see references in main text), ridge spreading rates, and long term estimates of plate motions from NUVEL-1A (DeMets *et al.* 1994) used in this study are represented as light blue lines. Large yellow stars denote the segments used to determine the stress field boundary conditions (see Section 3.3 and Fig. 4), small yellow stars denote the internal 'ring' segments. Boundary segments are calculated relative to the fixed reference point denoted by the blue star. Numbered areas correspond to Table 1. Background is shaded relief bathymetry and topography.

strain rates (block-like) (e.g. McCaffrey 2005) to concentrated zones of shear, the stresses throughout the plate boundary zone are spatially continuous.

There are three accepted driving forces for continental deformation in western North America (Richardson & Reding 1991; Sonder & Jones 1999): boundary forces (Atwater 1970; Stock & Molnar 1988; Bohannon & Parsons 1995), buoyancy forces (Fleitout & Froidevaux 1982; Fleitout 1991; Jones *et al.* 1996; Flesch *et al.* 2000; Townsend & Sonder 2001), and basal drag (McKenzie 1969; Tovish *et al.* 1978). It has been suggested that the relative motion between the Pacific and North American Plates could have led to extension within the Basin and Range (Atwater 1970). However, Sonder & Jones (1999) argued that stresses associated with relative plate motions alone are not large enough to drive extension but do contribute to it. Basal shear stresses generated from the subduction of the Farallon plate (McKenzie 1969), for

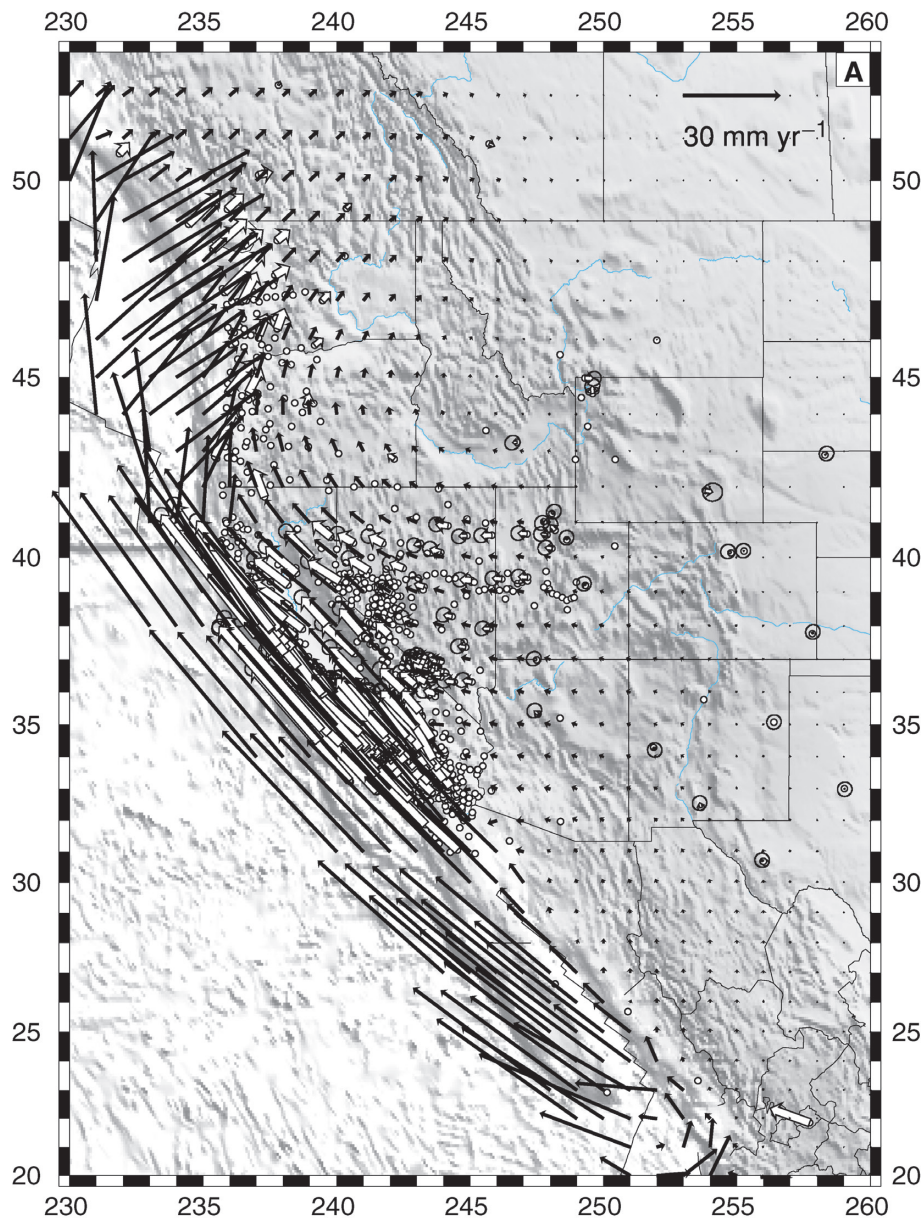


Figure 2. (a) The continuous model velocity field (black vectors), and GPS data (white vectors) from Bennett *et al.* (1999) plotted relative to a North American frame of reference. The remaining GPS and VLBI data [IGS; USGS; SCEC; Sauber *et al.* (1997); Ma & Ryan (1998); Antonelis *et al.* (1999); Bennett *et al.* (1999); Freymueller *et al.* (1999); Khazaradze *et al.* (1999); Dixon *et al.* (2000); Gan *et al.* (2000); McCaffrey *et al.* (2000); Oldow (2003) used in this model are plotted as white dots (without vectors) for clarity. Error ellipses represent the 95 per cent confidence limits. (b) Same as in (a) only shown for the Alaska/Canadian Rockies portion of the model. (c) The continuous model strain rate field associated with the model velocity field in Fig. 2(a). Principal axes of the strain rates are plotted as unit tensors with the second invariant of strain rate plotted in the background grid. Open arrows represent principal axes of extensional strain, closed arrows represent principal axes of compressional strain. (d) Same as in (c) only shown for the Alaska/Canadian Rockies portion of the model.

example, may aid extension but again are not large enough to drive extension (Wdowinski & O'Connell 1991). Jones *et al.* (1996) suggested that gravitational potential energy (GPE) differences due to lateral density variations within the lithosphere (Dalmayrac & Molnar 1981; Molnar & Lyon-Caen 1988) are large enough to drive all active extension in the western United States, excluding strike slip motion. Flesch *et al.* (2000) quantified the deviatoric stresses associated with buoyancy forces (GPE differences) and showed that these stresses are of comparable magnitude to the deviatoric stresses associated with accommodation of relative plate motions within the southwest United States. Although they argued that these two sources of deviatoric stress act approximately equally, and can explain the majority of deformation occurring within the southwestern United States, they ignored the potential contribution from basal tractions.

Recently, Silver & Holt (2002) directly solved for the mantle flow field beneath the southwestern United States using constraints from both shear wave splitting observations and surface relative motions. They concluded that the mantle flow is in the opposite direction to North America motion in a hotspot frame and is likely decoupled from the surface deformation field above. By contrast, Liu & Bird (2002) argued

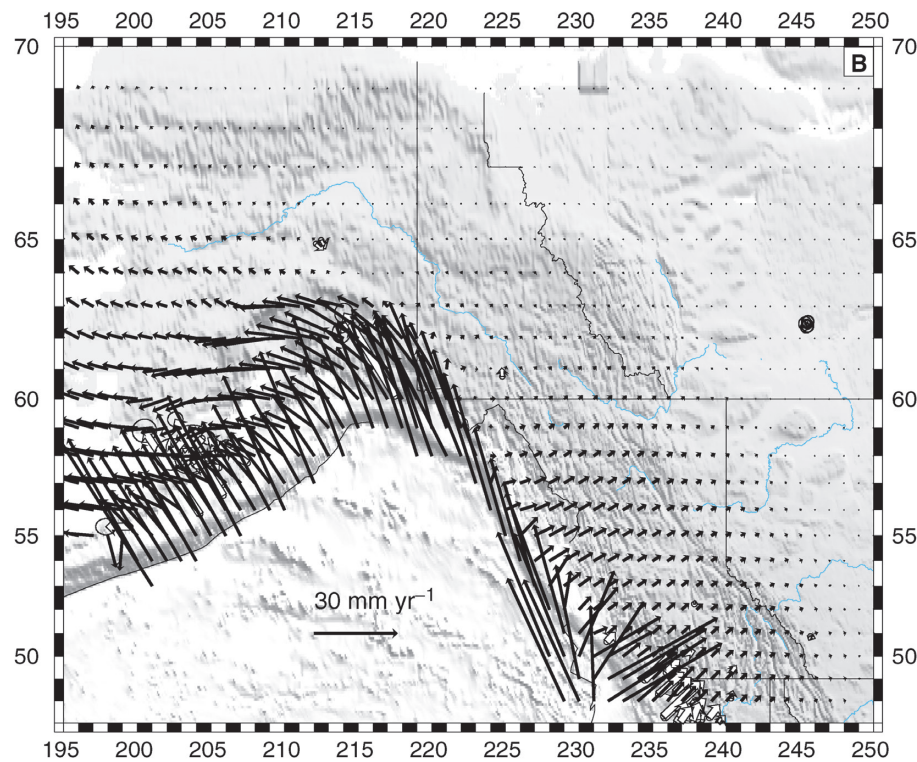


Figure 2. (Continued.)

that in order to obtain a fit to GPS velocities, plate motion models and spreading rates, their dynamic solution needed to contain westward active drag of North America as well as westward drag within the plate boundary zone itself. In order to understand the relative role of the deformational driving forces, we take a continuum physics approach to model the entire western North America Plate boundary zone and quantify the long-term vertically averaged deviatoric stress field arising from gravitational potential energy (GPE) variations within the lithosphere (buoyancy forces), effects of relative plate motions (boundary forces) and basal tractions.

2 KINEMATIC MODELING

We first seek a best estimate of the long-term continuous kinematic velocity and strain rate tensor field from geological and geodetic data, which will provide important constraints for the dynamic solution that we quantify. Recent studies (Pollitz 2003; Hetland & Hager 2004) have discussed transient behaviour in relation to GPS measurements. These transients can lead to errors in the magnitude estimate and spatial distribution of the long-term strain rate field. We therefore, also rely on geological quaternary fault slip rate data (Fig. 1) and long-term spreading estimates to help define the magnitude and style of the strain rate field. We use the strain rate tensor style (strike-slip, oblique slip, thrust and normal) and directions of strain rate principal axes to infer style and directions of deviatoric stresses responsible for long-term deformation; the magnitudes of strain rate are not used in this paper to constrain the dynamic solution. The main obstacle in using GPS data to define the expected styles of long-term deformation and the expected directions of principal axes results from the smearing effects of elastic versus permanent strain. South of the Cascadia subduction zone, within the strike-slip dominated portion of the plate boundary zone, Shen-Tu *et al.* (1999) have shown that the velocity fields and strain rate fields obtained from quaternary faults alone and GPS alone are similar when compared over length scales a few times the elastic thickness of the crust. We are considering such length scales here. Therefore, we feel confident that the GPS data south of the Medicine Triple Junction, taken together with quaternary fault slip rates, provide a first-order constraint on the long-term strain rate tensor field, when such rates are averaged within areas that are of a dimension several times the elastic thickness of the crust.

Another obstacle in using GPS data, just mentioned, is the effect transient deformation has on altering directions of principal axes of strain rate away from the long-term directions. Since we are seeking large-scale dynamic models, a diminished resolution in the spatial accuracy of the inferred long-term deformation field is not significant enough to entirely reject the use of GPS as a general indicator of both deformation style and direction of shortening and extension, except possibly in areas such as Cascadia, which we will discuss later. There non-permanent locking of the subduction zone may result in considerable differences in style between the short- and long-term strain rate fields.

We follow the method of Haines & Holt (1993) and Haines *et al.* (1998) using GPS and VLBI data (International GNSS Service available at: <http://sideshow.jpl.nasa.gov/mbh/series.html>, herein referred to as IGS; United States Geological Survey available at: <http://quake.usgs.gov/QUAKES/geodetic/gps> herein referred to as USGS; Southern California Earthquake Center available at: <http://www>).

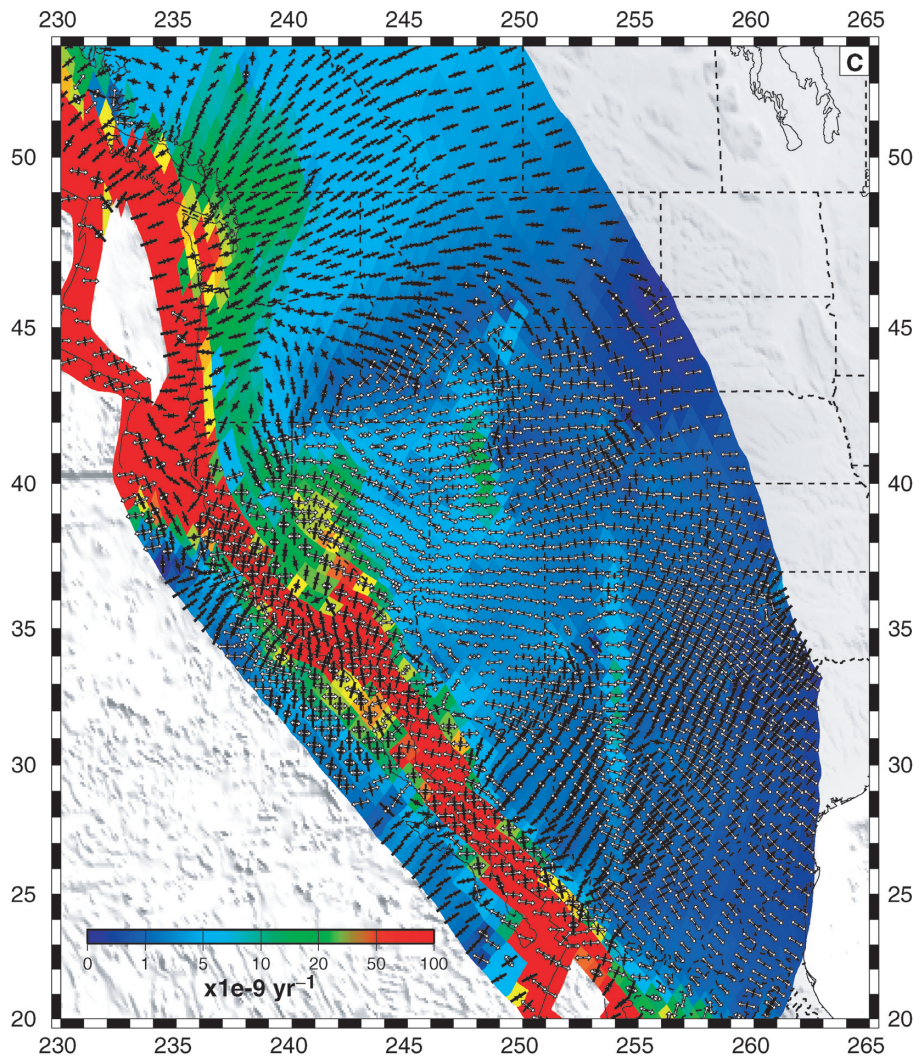


Figure 2. (Continued.)

scedc/sec/org/group_e/release.v2, herein referred to as SCEC3.0; Dixon *et al.* 1996, 2000; Sauber *et al.* 1997; Ma & Ryan 1998; Antonelis *et al.* 1999; Bennett *et al.* 1999; Freymueller *et al.* 1999; Khazaradze *et al.* 1999; Gan *et al.* 2000; McCaffrey *et al.* 2000; Bennett *et al.* 2001, 2003; Lavallee *et al.* 2001; McClusky *et al.* 2001; Miller *et al.* 2001a,b; Prescott *et al.* 2001; Svarc *et al.* 2002a,b; Oldow 2003; Savage *et al.* 2004), quaternary fault slip rate data (DeMets & Stein 1990; Wilson 1993; DeMets *et al.* 1994; Jennings 1994; Petersen & Wesnousky 1994; Plafker & Berg 1994; DeMets 1995; Bird 1996; DeMets & Dixon 1999; Shen-Tu *et al.* 1999), ridge spreading rates and long-term estimates of plate motions from NUVEL-1A (DeMets *et al.* 1994) to quantify a velocity gradient tensor (Figs 2a and b) and strain rate tensor (Figs 2c and d) field for the entire western North American Plate boundary zone. (Model fits to the GPS data are shown in Supplementary Fig. S1 and Supplementary Tables S1 and S2.)

There are two cases where such a strain rate tensor field poses problems as a proxy for the directions and styles of deviatoric stresses responsible for long-term permanent deformation: (1) regions in Oregon and Washington states that are affected by strain accumulation associated with the locked Juan de Fuca plate as it subducts beneath these regions (e.g. McCaffrey *et al.* 2000; Miller *et al.* 2001a) and (2) low strain rate regions (less than five nanostrain per year—Figs 2b and c). We will discuss such problem areas in the kinematic solution when we compare the final deviatoric stress field with the relative magnitudes of principal strain rates. Later we will argue for the need to remove GPS in Oregon and Washington from the kinematic solution in order to estimate a more reliable long-term kinematic field.

3 DYNAMIC MODELING

3.1 The force balance equations and the method of solving them

In solving for the deviatoric stress field associated with GPE variations in the lithosphere we follow the method of Flesch *et al.* (2001) and treat the lithosphere as continuous in stress. Because there are not enough geological and geodetic data to constrain strain rate as a function

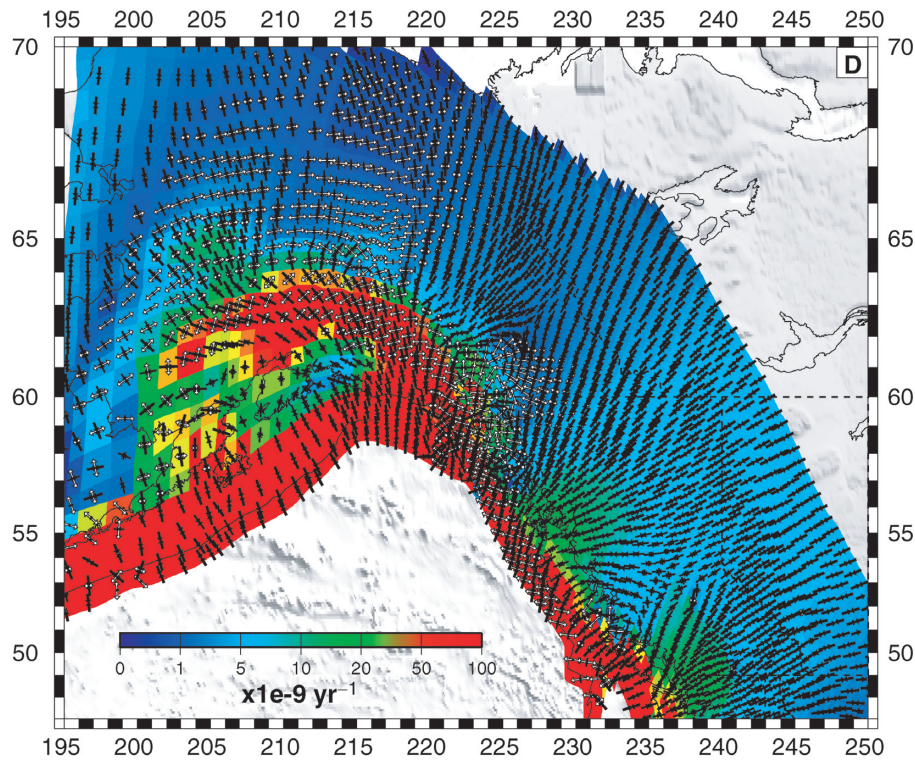


Figure 2. (Continued.)

of depth over the entire plate boundary zone we use the thin sheet approximation (Bird & Piper 1980; England & McKenzie 1982; England & Houseman 1986) to solve for the vertically averaged deviatoric stress field. However, in contrast to standard thin sheet approaches, we do not assume a specific viscous rheology or viscosity distribution to solve for the stress field solution. Instead we show that the force-balance equations can be separated into homogeneous and non-homogeneous parts, and these can be solved directly for minimum-magnitude deviatoric stress fields. The two solutions are then combined to provide a robust estimate of the total magnitude and style of the vertically averaged deviatoric stresses currently acting within the plate boundary zone of Western North America.

The force balance equations that we solve are for a spherical earth but for simplicity we provide the equations in Cartesian form:

$$\frac{\partial \sigma_{ij}}{\partial x_j} + \rho g_i = 0, \quad (1)$$

where ρ is the density, g is acceleration of gravity and σ_{ij} is the total stress tensor defined by

$$\sigma_{ij} = \tau_{ij} + \frac{\sigma_{kk}}{3} \delta_{ij} = \tau_{ij} + (\sigma_{zz} - \tau_{zz}) \delta_{ij}. \quad (2)$$

Here τ_{ij} is the deviatoric stress tensor, σ_{kk} is the trace of the total stress tensor and δ_{ij} is the Kronecker delta function. This definition of deviatoric stress in eq. (2) is the 3-D definition and is the same treatment used by Flesch *et al.* (2000) and Ghosh *et al.* (2006) who both point out the differences between the 2-D and 3-D treatments of deviatoric stress. Substituting (2) into (1) we can write the full force balance equations as

$$\frac{\partial \tau_{xx}}{\partial x} + \frac{\partial \sigma_{zz}}{\partial x} - \frac{\partial \tau_{zz}}{\partial x} + \frac{\partial \tau_{xy}}{\partial y} + \frac{\partial \tau_{xz}}{\partial z} = 0 \quad (3)$$

$$\frac{\partial \tau_{xy}}{\partial x} + \frac{\partial \sigma_{zz}}{\partial y} + \frac{\partial \tau_{yy}}{\partial y} - \frac{\partial \tau_{zz}}{\partial y} + \frac{\partial \tau_{yz}}{\partial z} = 0 \quad (4)$$

$$\frac{\partial \tau_{xz}}{\partial x} + \frac{\partial \tau_{yz}}{\partial y} + \frac{\partial \sigma_{zz}}{\partial z} = -\rho g. \quad (5)$$

If the horizontal gradients in shear tractions τ_{xz} and τ_{yz} are small compared to ρg , then from eq. (5)

$$\frac{\partial \tau_{xz}}{\partial x} + \frac{\partial \tau_{yz}}{\partial y} \ll \rho g$$

and

$$\sigma_{zz}(z) = - \int_{-h}^z \rho(z') g dz' \quad (6)$$

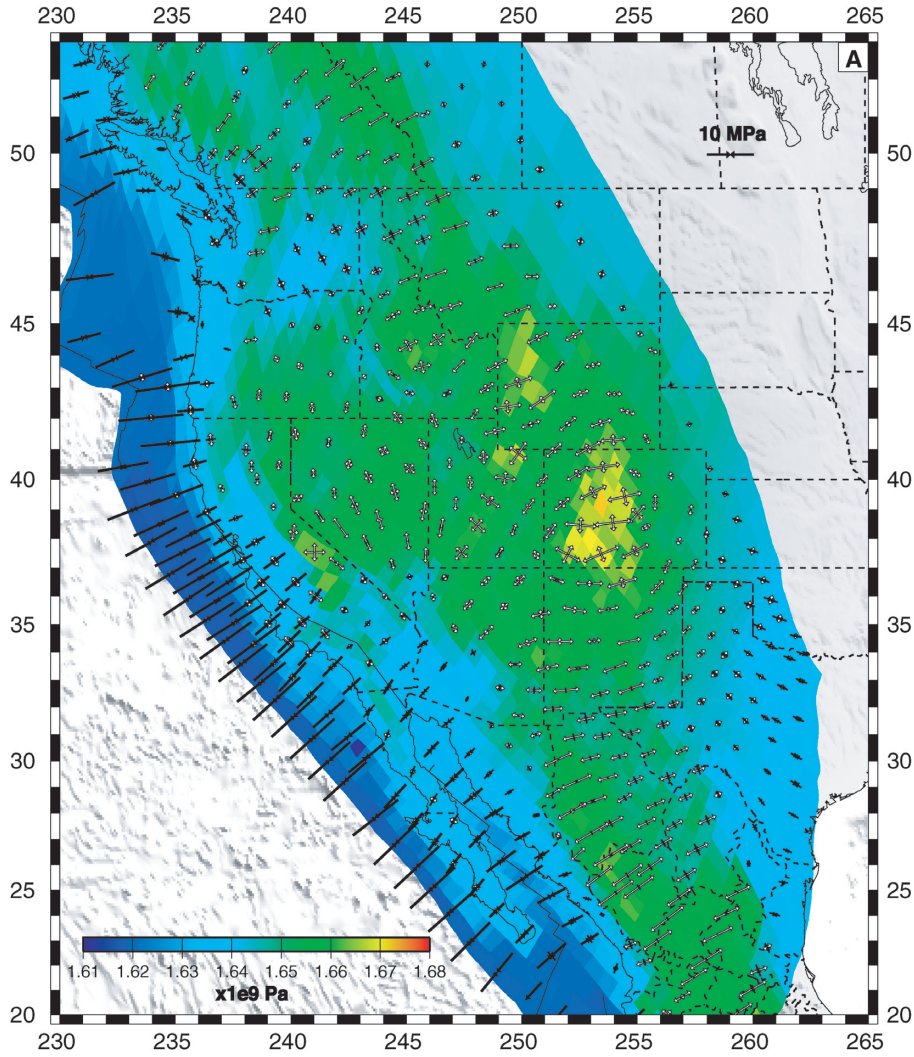


Figure 3. (a) The vertically averaged deviatoric stress field associated with gravitational potential energy variations in the lithosphere for the western United States portion of the model. Gravitational potential energy estimates were determined assuming the lithosphere is in Airy isostatic balance and are plotted in the colour background. Open arrows represent tensional principal axes of deviatoric stress, closed arrows represent compressional principal axes of deviatoric stress. (b) Same as in (a) only shown for the Alaska/Canadian Rockies portion of the model. (c) Same as in (a) only gravitational potential energy estimates were determined using the CRUST2.0 data set. (d) Same as in (c) only shown for the Alaska/Canadian Rockies portion of the model.

and we are left with only eqs (3) and (4) to solve. Because the horizontal length scales of the plate boundary zone are large compared to the lithospheric thickness, we choose to vertically integrate eqs (3) and (4) and then solve these equations directly for the vertically averaged deviatoric stresses. The vertically averaged eqs (3) and (4), from the surface at $z = -h$, where h is the surface elevation, to the base of the lithosphere at a uniform depth $z = L$, are

$$\frac{\partial \bar{\tau}_{xx}}{\partial x} - \frac{\partial \bar{\tau}_{zz}}{\partial x} + \frac{\partial \bar{\tau}_{xy}}{\partial y} = -\frac{\partial \bar{\sigma}_{zz}}{\partial x} - \frac{1}{L} \tau_{xz}(L) \quad (7)$$

$$\frac{\partial \bar{\tau}_{xy}}{\partial x} - \frac{\partial \bar{\tau}_{zz}}{\partial y} + \frac{\partial \bar{\tau}_{yy}}{\partial y} = -\frac{\partial \bar{\sigma}_{zz}}{\partial y} - \frac{1}{L} \tau_{yz}(L), \quad (8)$$

where $\tau_{xz}(L)$ and $\tau_{yz}(L)$ are the tractions applied to the base of the lithosphere that fall out of the vertical integrals [$\tau_{xz}(-h)$ and $\tau_{yz}(-h)$ are zero]. The vertically averaged stresses, $\bar{\tau}_{ij}$ and $\bar{\sigma}_{zz}$, obtained by dividing the corresponding depth integrals by the reference lithospheric thickness L , are defined as

$$\bar{\tau}_{ij} = \frac{1}{L} \int_{-h}^L \tau_{ij} dz \quad (9)$$

$$\bar{\sigma}_{zz} = -\frac{1}{L} \int_{-h}^L \left[\int_{-h}^z \rho(z') g dz' \right] dz = -\frac{1}{L} \int_{-h}^L (L-z) \rho(z) g dz. \quad (10)$$

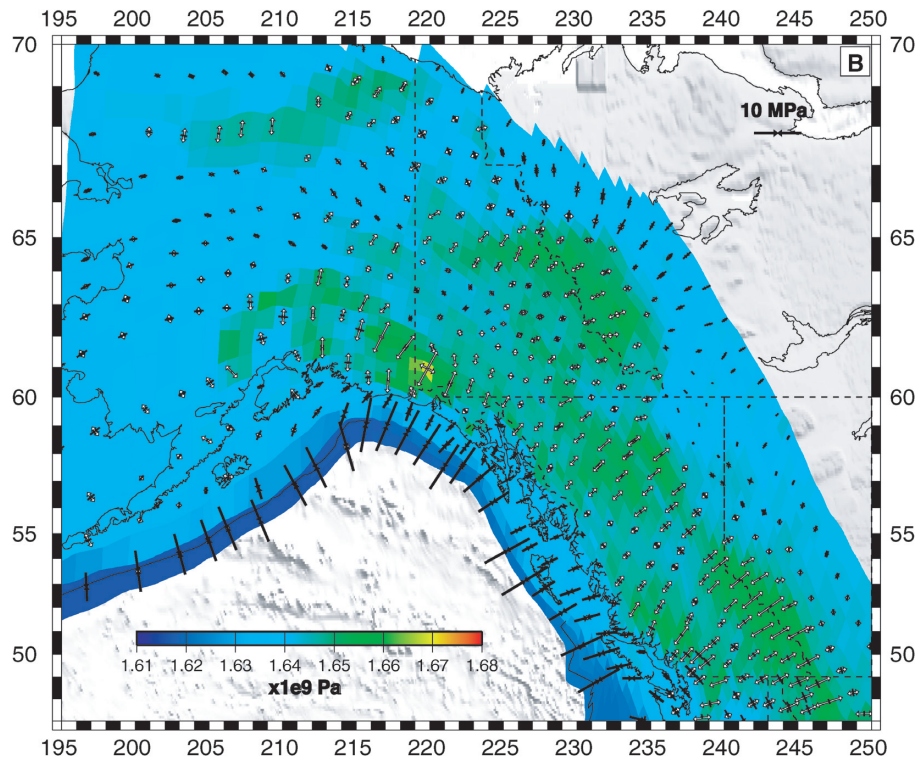


Figure 3. (Continued.)

The vertically averaged vertical stress defined in eq. (10) is equivalent to $1/L$ times the gravitational potential energy per unit area defined with the reference level at the base of the lithosphere at depth L , and herein will be referred to as GPE. This reference level in eq. (10) is the only appropriate reference level to use in application to the thin sheet approach of solving the force balance equations. This reference level differs from that of Fleitout & Froidevaux (1982), Fleitout (1991) and Zoback & Mooney (2003). However, eq. (10) is equivalent to earlier definitions for GPE described within those studies so long as the pressure at the reference level, L , is everywhere constant (i.e. isostatic compensation with no sources of dynamic topography).

The terms on the right hand sides of (7) and (8), tractions applied to the base of the lithosphere and horizontal gradients in GPE, respectively, are equivalent to body force terms. These body force terms are balanced by gradients in the horizontal deviatoric stresses. Writing eqs (7) and (8) in summation notation

$$\frac{\partial}{\partial x_{\beta}}(\bar{\tau}_{\alpha\beta} + \delta_{\alpha\beta} \bar{\tau}_{\gamma\gamma}) + f_{1\alpha} + f_{2\alpha} = 0, \quad (11)$$

where $\bar{\tau}_{\alpha\beta}$ is the vertically averaged horizontal deviatoric stress tensor (i.e. xx , xy , yx and yy components) and, $\bar{\tau}_{\gamma\gamma} = \bar{\tau}_{xx} + \bar{\tau}_{yy} = -\bar{\tau}_{zz}$. The summation is performed over the repeated index, β ; the indices, α and β , vary over $x_1 = x$ and $x_2 = y$ directions, and $f_{1\alpha} = \frac{\partial \bar{\sigma}_{zz}}{\partial x_{\alpha}}$ and $f_{2\alpha} = \frac{1}{L} \tau_{x_{\alpha}z}$. The distribution of the body force terms embedded in equations in (11) can be estimated directly from geophysical observations.

The GPE values, $\bar{\sigma}_{zz}$, can be estimated from topography data and seismically defined crustal thickness variations. The definition of the geoid is different than eq. (10). The geoid is only appropriate to use as a proxy for GPE if all topography is in isostatic balance (Haxby & Turcotte 1978) at the reference level, L , and there is no dynamic topography (Appendix A). That is, the definition relating the geoid to GPE is only correct when the pressure at the base of the lithosphere is everywhere constant, implying that all topography is isostatically compensated and no dynamic topography contributes (see Appendix A for the mathematical explanation). This is unlikely to be the case for western North America (Lowry *et al.* 2000; Panasyuk & Hager 2000). Therefore, we do not use the geoid to estimate GPE. However, for cases in which the pressure at the reference level, L , varies over long-wavelengths, then the shorter-wavelength variations in the geoid can likely be used as a proxy for shorter wavelength variations in GPE.

The basal traction terms can be inferred from 3-D mantle circulation models that are constrained by geoid, topography, plate motions, and density buoyancy distributions, which are inferred from the history of subduction and seismic tomography models (e.g. Wen & Anderson 1997a,b). These observationally defined distributions of body forces must satisfy equations in (11).

The equations in (11) can be separated into three equations, two non-homogeneous differential equations and one homogeneous equation

$$\frac{\partial}{\partial x_{\beta}}(\bar{\tau}_{\alpha\beta} + \delta_{\alpha\beta} \bar{\tau}_{\gamma\gamma}) = -f_{1\alpha} \quad (12)$$

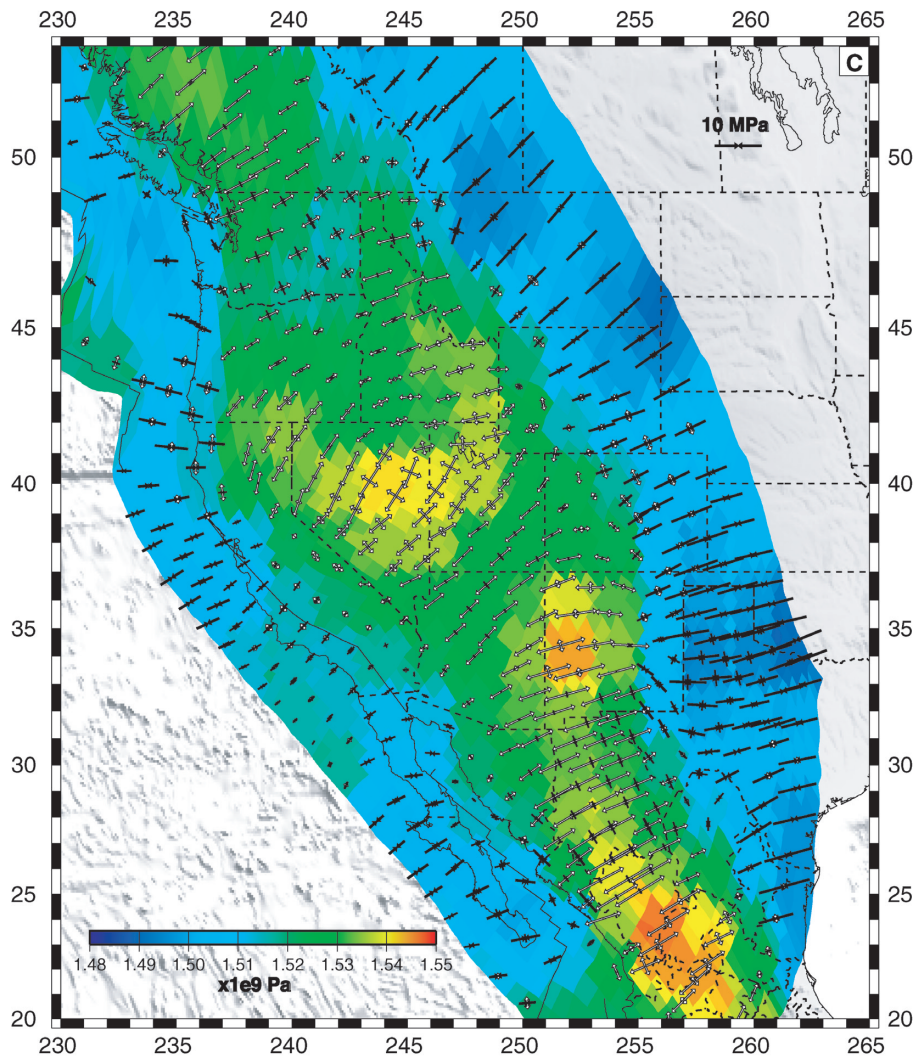


Figure 3. (Continued.)

$$\frac{\partial}{\partial x_\beta} (\bar{\tau}_{\alpha\beta} + \delta_{\alpha\beta} \bar{\tau}_{\gamma\gamma}) = -f_{2\alpha} \quad (13)$$

$$\frac{\partial}{\partial x_\beta} (\bar{\tau}_{\alpha\beta} + \delta_{\alpha\beta} \bar{\tau}_{\gamma\gamma}) = 0, \quad (14)$$

with solutions to (14) being obtained with stress boundary conditions to approximate the influence that density buoyancy distributions (both lithospheric GPE and basal tractions) everywhere outside the region of interest have on the plate boundary zone region. Solutions $(\bar{\tau}_{xx}, \bar{\tau}_{yy}, \bar{\tau}_{xy})$ to these equations can be obtained separately and then added to one another, since the equations are linear in stress.

The equations in (12), (13) and (14) are underdetermined with three unknowns but only two equations. Flesch *et al.* (2001) demonstrated a method to obtain a unique mathematical solution to (12)–(14) by imposing a constraint that the solution that balances the distribution of body forces possesses the minimum possible surface integral of the second invariant of stress. Thus, in a mathematical sense we are solving for the minimum deviatoric stress field solution that is a physical approximation: it implicitly assumes a linear uniform rheology. Flesch *et al.* (2001) have shown that, although this is an approximation to the exact rheology, the exact mathematical solution from this method yields deviatoric stresses for Asia that agree to within a factor of two or better with a solution obtained using the same GPE distribution, but with variable non-linear viscosity and with applied velocity boundary conditions. The following functional is minimized in the present, more approximate technique:

$$I = \int_S [\bar{\tau}_{\alpha\beta} \bar{\tau}_{\alpha\beta} + (\bar{\tau}_{\gamma\gamma}^2)] dS + \int_S 2\lambda_\alpha \left[\frac{\partial}{\partial x_\beta} (\bar{\tau}_{\alpha\beta} + \delta_{\alpha\beta} \bar{\tau}_{\gamma\gamma}) + f_{1\alpha} + f_{2\alpha} \right] dS, \quad (15)$$

where S is the area of the Earth's surface being considered. Optimization of eq. (15) involves the minimization of the second invariant of the stress field (first integral), subject to the constraint that this stress field satisfies the force balance equations (eqs 12–14) (second integral), where $\Lambda = (\lambda_x, \lambda_y)$ are Lagrange multipliers for the force-balance constraint. The application of constraints using Lagrange multipliers is

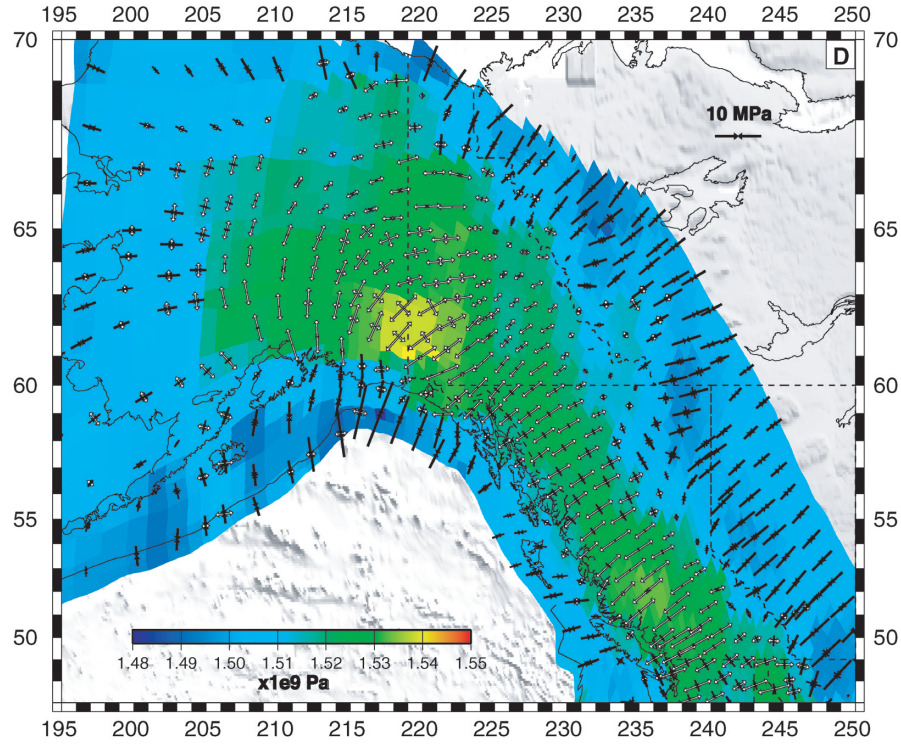


Figure 3. (Continued.)

commonly used in dealing with underdetermined systems (e.g. Menke 1982). Using the variational principle (e.g. Morse & Feshbach 1953) to optimize (15) with respect to $\bar{\tau}_{\alpha\beta}$ (see Flesch *et al.* 2001) Appendix A for details) yields a relationship between stress and the Lagrange multipliers,

$$\bar{\tau}_{\alpha\beta} = \frac{1}{2} \left(\frac{\partial \lambda_{\alpha}}{\partial x_{\beta}} + \frac{\partial \lambda_{\beta}}{\partial x_{\alpha}} \right) \quad (16)$$

at all points inside S , and $\Lambda = (\lambda_x, \lambda_y) = 0$ at all points on the boundary ∂S . That is, $\bar{\tau}_{\alpha\beta}$ is related to the vector of Lagrangian multipliers $\Lambda = (\lambda_x, \lambda_y)$ in the same way that strain rate $\dot{\epsilon}_{\alpha\beta}$ is related to the velocity vector $\underline{v} = (u_x, u_y)$. Substituting eq. (16) into eq. (11) gives the force-balance equations that the Lagrange multipliers, $\Lambda = (\lambda_x, \lambda_y)$, have to satisfy:

$$\frac{\partial}{\partial x_{\beta}} \left[\frac{1}{2} \left(\frac{\partial \lambda_{\alpha}}{\partial x_{\beta}} + \frac{\partial \lambda_{\beta}}{\partial x_{\alpha}} \right) + \delta_{\alpha\beta} \frac{\partial \lambda_{\gamma}}{\partial x_{\gamma}} \right] = -f_{1\alpha} - f_{2\alpha}, \quad (17)$$

where $\partial \lambda_{\gamma} / \partial x_{\gamma} = \partial \lambda_x / \partial x + \partial \lambda_y / \partial y$. Therefore, with a lateral estimate of GPE or basal tractions, we can directly solve eq. (17) to determine a vertically averaged deviatoric stress field associated with body force distributions within the lithosphere and basal tractions applied to the base of the lithosphere (Figs 3 and 7). We are able to solve the equations in (17) through the minimization of the functional

$$J = \int \left\{ \left[\begin{array}{c} \frac{\partial \lambda_x}{\partial x} \\ \frac{\partial \lambda_y}{\partial y} \\ \frac{1}{2} \left(\frac{\partial \lambda_x}{\partial y} + \frac{\partial \lambda_y}{\partial x} \right) \end{array} \right] - \left[\begin{array}{c} \Phi_{xx} \\ \Phi_{yy} \\ \Phi_{xy} \end{array} \right] \right\}^T \left[\begin{array}{ccc} 2 & 1 & 0 \\ 1 & 2 & 0 \\ 0 & 0 & 2 \end{array} \right] \left\{ \left[\begin{array}{c} \frac{\partial \lambda_x}{\partial x} \\ \frac{\partial \lambda_y}{\partial y} \\ \frac{1}{2} \left(\frac{\partial \lambda_x}{\partial y} + \frac{\partial \lambda_y}{\partial x} \right) \end{array} \right] - \left[\begin{array}{c} \Phi_{xx} \\ \Phi_{yy} \\ \Phi_{xy} \end{array} \right] \right\} dS, \quad (18)$$

where Φ_{xx} , Φ_{yy} and Φ_{xy} are potentials consisting of integrals of the body forces. In the case of gravitational potential energy fields, or tractions associated with poloidal flow fields

$$\Phi_{xx} = -\frac{2}{3} \int f_x dx + \frac{1}{3} \int f_y dy, \quad \Phi_{yy} = \frac{1}{3} \int f_x dx - \frac{2}{3} \int f_y dy, \quad \Phi_{xy} = 0.$$

Flesch *et al.* (2001) have shown that the minimization of the functional J above provides a solution to the force balance equations in (17) and is equivalent to the optimization of (15). Note that in the case of calculating deviatoric stresses associated with GPE variations, the potentials in (18) take the form of $\Phi_{xx} = \Phi_{yy} = -\bar{\sigma}_{zz}/3$ and in the case of tractions associated with mantle circulation patterns the potentials consist of horizontal integrals of the applied shear tractions.

3.2 Deviatoric stresses associated with GPE in western North America

The magnitudes and distribution of GPE calibrate the magnitude of deviatoric stress acting in the lithosphere. We estimate GPE (Figs 3a–d) from two different data sets. First, we used the ETOPO5 topography data set, and make the assumptions that the lithosphere is in Airy isostatic

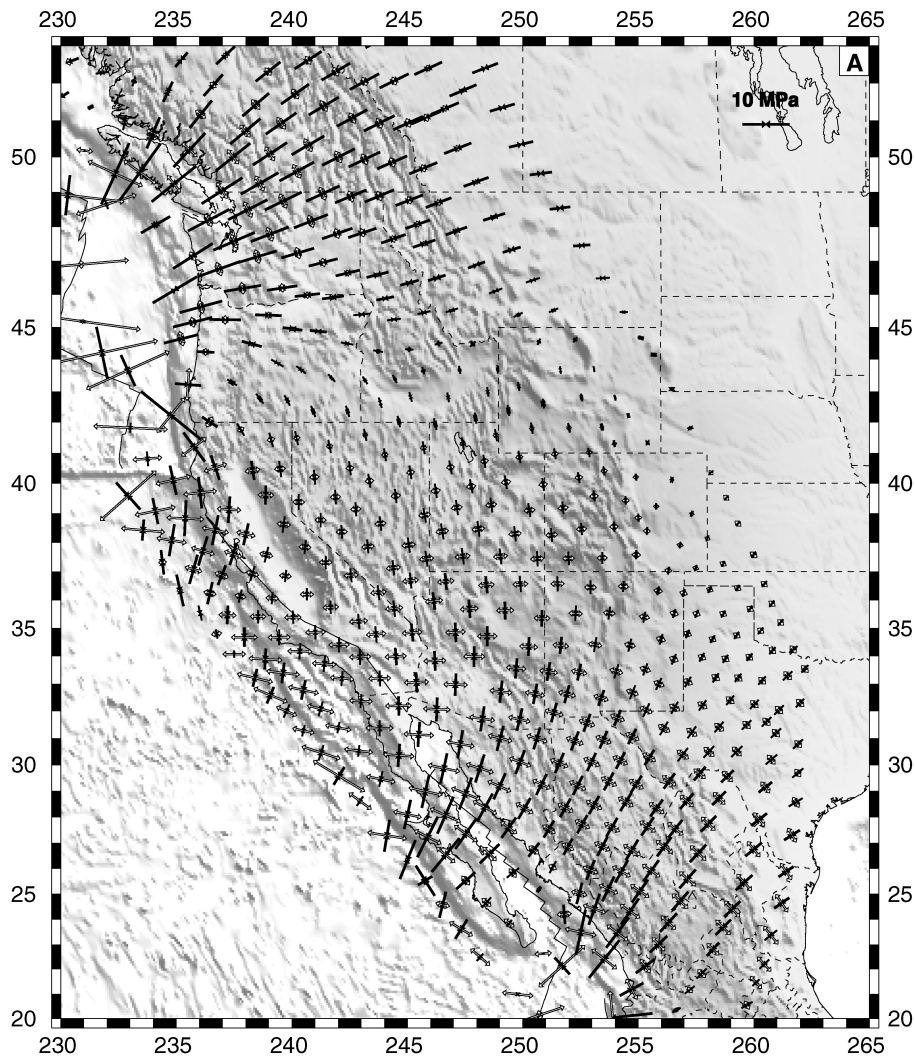


Figure 4. (a) The best-fitting stress field boundary condition using GPE estimates assuming Airy isostatic balance, for the western United States portion of the model. Open arrows represent principal axes of tensional deviatoric stress, closed arrows represent principal axes of compressional deviatoric stress. (b) Same as shown in (a) only for the Alaska/Canadian Rockies portion of the model. (c) Same as shown in (a) only for GPE estimates determined from the CRUST2.0 model. (d) Same as shown in (c) only for the Alaska/Canadian Rockies portion of the model.

balance with average crustal and mantle densities of 2750 kg m^{-3} and 3300 kg m^{-3} , respectively. We then calculate a GPE estimate for each grid area using eq. (10); herein we refer to this GPE distribution as the Airy case. In the second method, we use the CRUST2.0 (Mooney *et al.* 1998) seismic crustal thickness model and eq. (10) to estimate GPE for each grid area. This GPE distribution will be referred to as the CRUST2.0 case. We adjust the mantle densities within each column to require that each lithospheric column is in isostatic balance. Although the pressure at the reference level, L , is unlikely to be a constant due to the presence of dynamic topography, we perform this correction in order to compare the derived GPE field from CRUST2.0 with the Airy model, which is also compensated (constant pressure at reference depth L). Compensated and uncompensated CRUST2.0 models yield vertically averaged deviatoric stress solutions that do not differ in style of stress, but only differ in magnitude by about 10 per cent (Ghosh *et al.* 2006).

We calculate the deviatoric stress field associated with these variations of $1/L$ times the gravitational potential energy per unit area (GPE estimates) by solving eq. (17) (with $f_{2\alpha} = 0$) through the minimization of (18). The two different GPE distributions produce similar first-order patterns of deviatoric stress in most regions: tensional deviatoric stress over regions of high relative GPE and deviatoric compression over regions of low relative GPE (Fig. 3). There are, however, significant differences between the two solutions that are related to differences in the two GPE field estimates. For example, within the Airy solution, the lowest GPE values, and generally highest magnitude of compressional deviatoric stress ($\sim 10 \text{ MPa}$), lie within the Pacific Plate at the western edge of the model (Figs 3a and b). On the other hand, for the CRUST2.0 solution, the lowest GPE values and largest magnitude of vertically averaged compressional deviatoric stress ($\sim 10 \text{ MPa}$), lie east of the Rockies at the edge of the Great Plains (Figs 3c and d). Note that all deviatoric stresses that we refer to are vertical averages of deviatoric stress

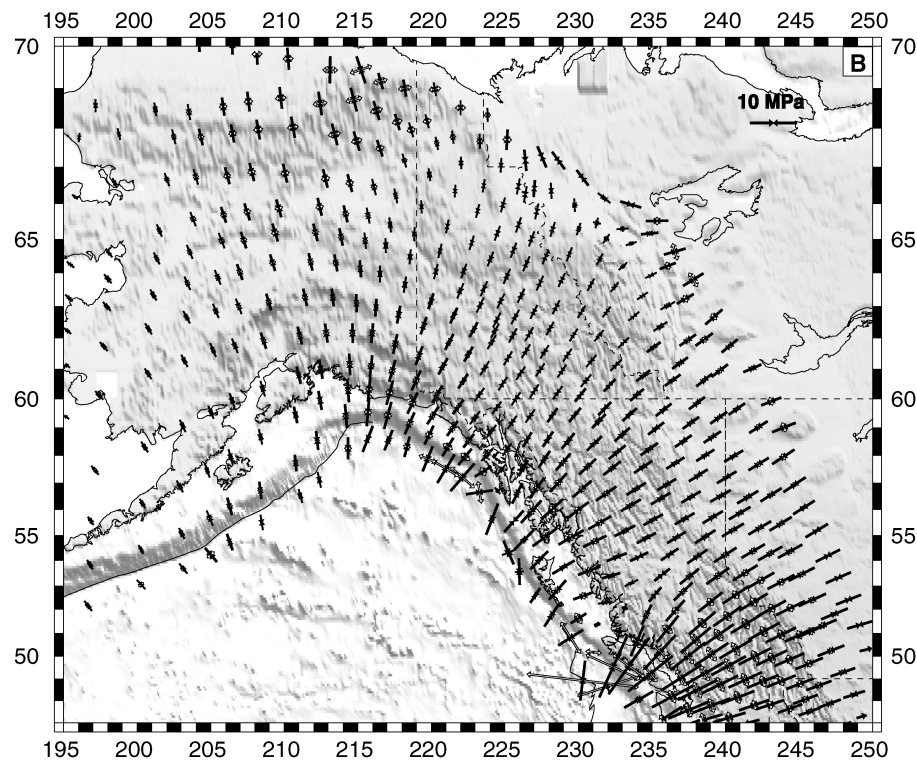


Figure 4. (Continued.)

obtained for a plate with a reference level at 100 km depth below sea level. In order to obtain vertically integrated magnitudes of deviatoric stress, with units of N m^{-1} , simply multiply given values of vertical average by 10^5 .

Additionally, in the Airy solution (Figs 3a and b) the highest GPE values are associated with the highest topography and the largest magnitudes of tensional deviatoric stresses (5–10 MPa) are generally associated with these high estimates of relative GPE. For the CRUST2.0 case (Fig. 3c) the highest values of GPE are not everywhere associated with the highest topography and instead occur within the Great Basin of Nevada and Utah, along a N–S trending ridge just west of the Rio Grande Rift within New Mexico, and along the high topography of Mexico (Fig. 3c).

Within the high ridge of GPE that spans Mexico, New Mexico and eastern Arizona, as well as throughout much of western Canadian Rockies and the high topography of Alaska, the directions for the principal axes of tensional deviatoric stress for both the Airy and CRUST2.0 solutions agree with one another (Figs 3a–d). The most significant difference between the tensional portions of the two solutions lies within the Great Basin of Utah and Nevada (Figs 3a and c). Here within the CRUST2.0 solution there is an E–W trending GPE high, which yields nearly pure isotropic patterns of deviatoric tension with maximum principal axes of deviatoric extensional stress oriented NE–SW along this ridge (Fig. 3c). Within the same region in the Airy solution, the directions of deviatoric tensional stresses are oriented roughly N–S. In general, the magnitude of deviatoric tensional stresses are larger from the GPE solution associated with the CRUST2.0 data set, with maximum differences in magnitude reaching a factor of two in some regions (e.g. eastern boundary of the grid as well as off the coast of California).

Differences in the absolute magnitudes of $1/L$ times the gravitational potential energy per unit area (GPE) for the Airy case (Fig. 3a) versus the CRUST2.0 case (Fig. 3c) are related primarily to differences in mantle densities for the two models. Mantle densities for the CRUST2.0 case (Mooney *et al.* 1998) are generally 100 kg m^{-3} lower than that assumed for the Airy topography model, thus yielding lower absolute values of GPE for the CRUST2.0 case. On the other hand, relative differences in GPE are greater for the CRUST2.0 case ($\sim 70 \text{ MPa}$) than for the Airy topography case ($\sim 60 \text{ MPa}$), which explains why, on average, the deviatoric stresses for the CRUST2.0 model are larger than for the Airy model by about 10–20 per cent.

The N–S to NE–SW direction of the deviatoric tensional stress in the Great Basin (Figs 3a and c) is not consistent with the predominantly E–W extensional strain directions there. It is therefore, clear that buoyancy forces alone are not enough to drive all of the extensional deformation or shear deformation within the western United States (e.g. Fleisch *et al.* 2000; Choi & Gurnis 2003).

3.3 Stress field boundary conditions and the total deviatoric stress field

The second step in estimating the deviatoric stress field, and lithospheric driving forces, involves solving for a stress field boundary condition. The force-balance equations in (17) are linear in stress, allowing any number of solutions to be added to determine a final stress field solution

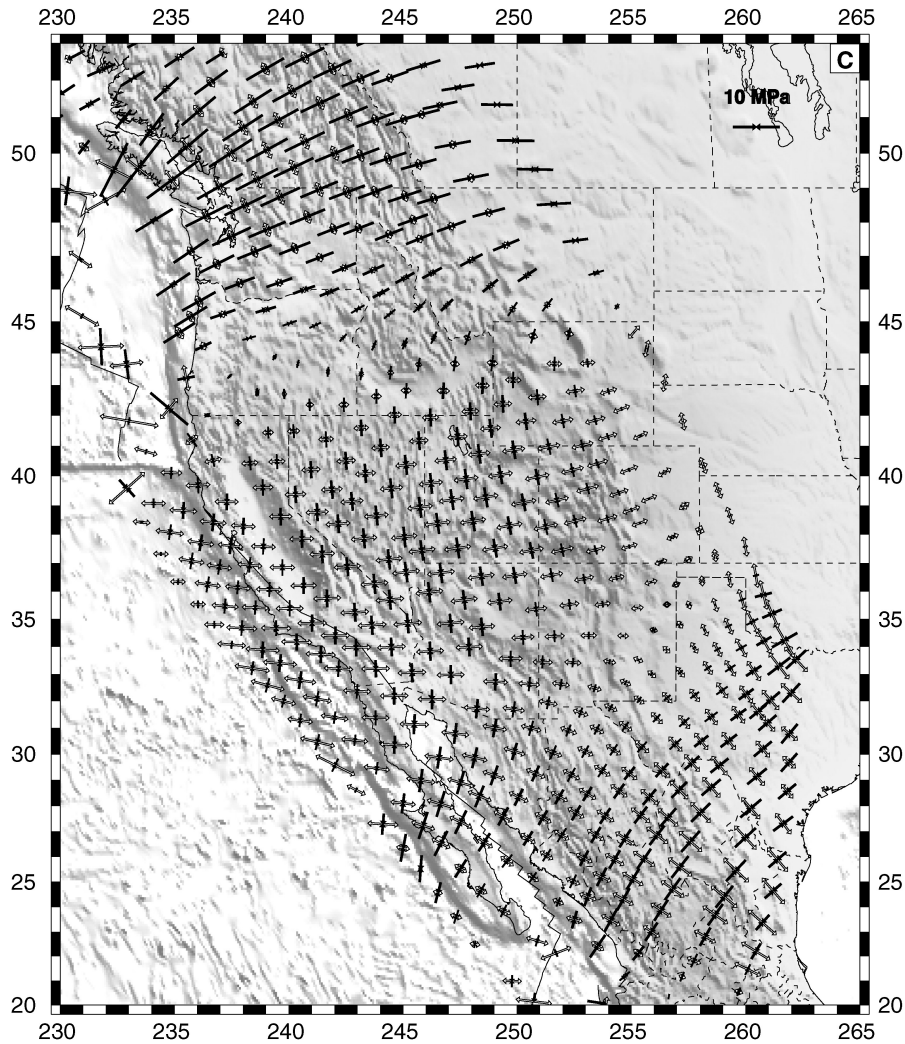


Figure 4. (Continued.)

(Flesch *et al.* 2001). A stress field boundary solution involves solving the homogeneous equations in (17) (setting both $f_{1\alpha}$ and $f_{2\alpha}$ to zero) (Flesch *et al.* 2001). This involves defining a continuous distribution of $\Lambda = (\lambda_x, \lambda_y)$ along the boundary, and then minimizing (18), thus providing a solution to the homogeneous equations in (17). The continuous boundary condition of $\Lambda = (\lambda_x, \lambda_y)$ is set up such that $\Lambda = \omega \times \mathbf{r}$, where \mathbf{r} is the radial vector that is located along the boundary and $\omega = (1, 0, 0)$, $(0, 1, 0)$ and $(0, 0, 1)$. A continuous distribution of Λ along the boundary is achieved by defining Λ at 56 points along the boundary (Fig. 1), which defines 56 segments. Cubic spline functions are used to interpolate $\Lambda = (\lambda_x, \lambda_y)$ values to ensure continuous smooth variation in Λ vector along the boundary. In addition, there are two ‘ring’ boundary segments with seven segments each that delineate the Juan de Fuca and Rivera plates within the interior of the grid, making a total of 70 segments. For each boundary segment we calculate the stress field response corresponding to the three values of ω , yielding a total of 210 (70 segments \times 3) stress field basis functions. The complete stress field boundary condition is the sum of stress field basis functions, calculated around the boundary of our grid. This stress field boundary condition is added to our deviatoric stress field associated with GPE effects

$$\tau = \tau_0 + \sum_{j=1}^{\text{nseg}} \sum_{i=1}^3 a_{ij} \tau_{ij}, \quad (19)$$

where τ_0 is the deviatoric stress tensor associated with GPE variations within the lithosphere (Fig. 3), a_{ij} are the scaling factors for the stress field basis functions, and τ_{ij} are the stress field basis functions. The 210 scaling factors, a_{ij} , (three for each boundary segment) are determined in an iterative least-squares inversion. The objective function we minimize is

$$\sum_{\text{areas}} \left\{ T - \frac{(e \cdot \tau)}{E} \right\} \Delta S, \quad (20)$$

where

$$E = \sqrt{\dot{\epsilon}_{xx}^2 + \dot{\epsilon}_{yy}^2 + \dot{\epsilon}_{zz}^2 + \dot{\epsilon}_{xy}^2 + \dot{\epsilon}_{yx}^2} = \sqrt{2\dot{\epsilon}_{xx}^2 + 2\dot{\epsilon}_{xx}\dot{\epsilon}_{yy} + 2\dot{\epsilon}_{yy}^2 + 2\dot{\epsilon}_{xy}^2},$$

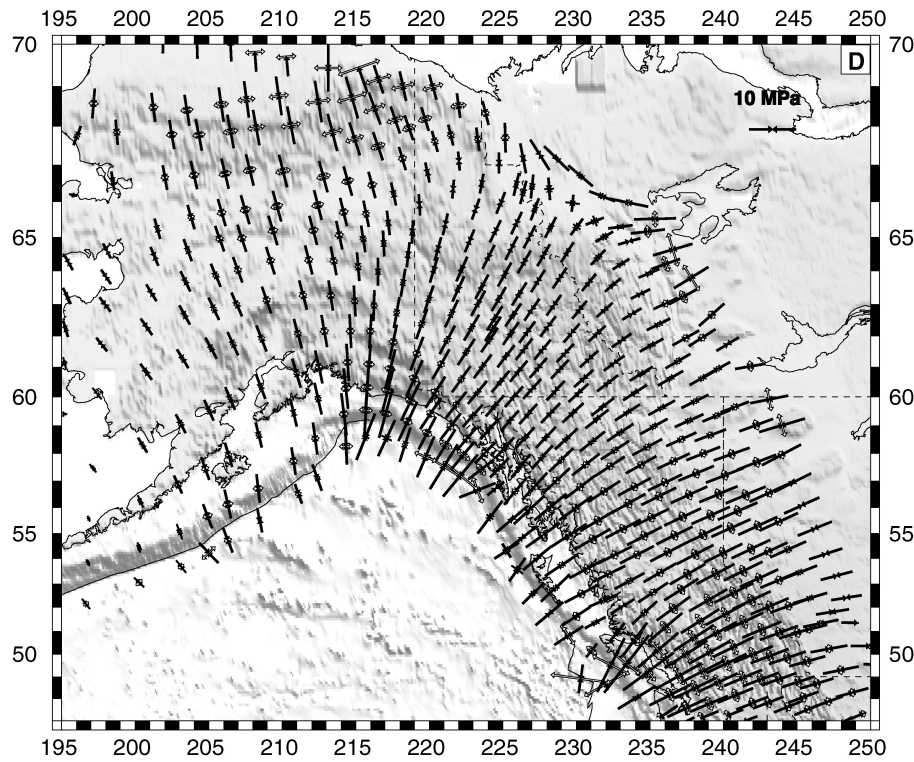


Figure 4. (Continued.)

$$T = \sqrt{\tau_{xx}^2 + \tau_{yy}^2 + \tau_{zz}^2 + \tau_{xy}^2 + \tau_{yx}^2} = \sqrt{2\tau_{xx}^2 + 2\tau_{xx}\tau_{yy} + 2\tau_{yy}^2 + 2\tau_{xy}^2},$$

$$e \cdot \tau = \dot{\epsilon}_{xx}\tau_{xx} + \dot{\epsilon}_{yy}\tau_{yy} + \dot{\epsilon}_{zz}\tau_{zz} + \dot{\epsilon}_{xy}\tau_{xy} + \dot{\epsilon}_{yx}\tau_{yx} = 2\dot{\epsilon}_{xx}\tau_{xx} + \dot{\epsilon}_{xx}\tau_{yy} + \dot{\epsilon}_{yy}\tau_{xx} + 2\dot{\epsilon}_{yy}\tau_{yy} + 2\dot{\epsilon}_{xy}\tau_{xy},$$

ΔS is the grid area, $\dot{\epsilon}_{ij}$ is the strain rate from the kinematic modelling (Figs 2c and d), and τ_{ij} is the total deviatoric stress tensor expressed in eq. (19). This objective function is minimized when the directions of principal axes of deviatoric stress are aligned with the directions of principal axes of strain rate and when the style of deformation predicted by the stress field (e.g. strike-slip, thrust, normal or a combination of these) matches the style of strain rate, with weighting factor T . That is, because we are looking at large scale features, when solving for the stress field boundary condition, we assume an isotropic relationship between stress and strain rate. Because the San Andreas Fault may be weak in the direction of slip, and thus anisotropic, grid areas containing the San Andreas Fault were not used in the inversion for a stress field boundary condition; however, we did include grid areas containing the Fairweather fault.

The minimization of (20) provides a unique global minimum. For dense distributions of basis functions, as we have used, the misfit vector $\hat{e} - \hat{\tau}$, where \hat{e} is the unit strain tensor and $\hat{\tau}$ is the unit stress tensor, is orthogonal to each of the basis solutions when integrated over the entire plate boundary zone.

The best-fitting stress field boundary conditions for both the Airy and CRUST2.0 cases (Fig. 4) have deviatoric stresses consistent with a right lateral shearing of the Pacific Plate past the North American Plate between the southern tip of Baja and the Mendocino Triple Junction (N–S deviatoric compression of 3–7 MPa and E–W tensional deviatoric stresses of 3–7 MPa). This shearing dies out rapidly north of the Mendocino Triple Junction. Within Mexico and the state of Texas the principal axes of compressional deviatoric stress are oriented NE–SW. North of the Mendocino Triple Junction, the boundary condition solution involves compressional deviatoric stresses (3–10 MPa) oriented roughly perpendicular to the coastline. Both boundary condition solutions for the Airy and CRUST2.0 cases are remarkably similar in terms of the style of deviatoric stress imposed within the plate boundary zone.

3.4 The total deviatoric stress field

The total vertically averaged deviatoric stress field (Fig. 5) is the sum of the stress field associated with GPE variations (Fig. 3) and the stress field associated with the boundary conditions (Fig. 4). The total deviatoric stress field (Fig. 5, Table 1) agrees with most of the deformation style occurring within western North America. This total deviatoric stress field in Fig. 5 is superimposed on a colour plot of the misfit function M

$$M = \frac{1}{2} \left(1 - \frac{\mathbf{e} \cdot \boldsymbol{\tau}}{ET} \right), \quad (21)$$

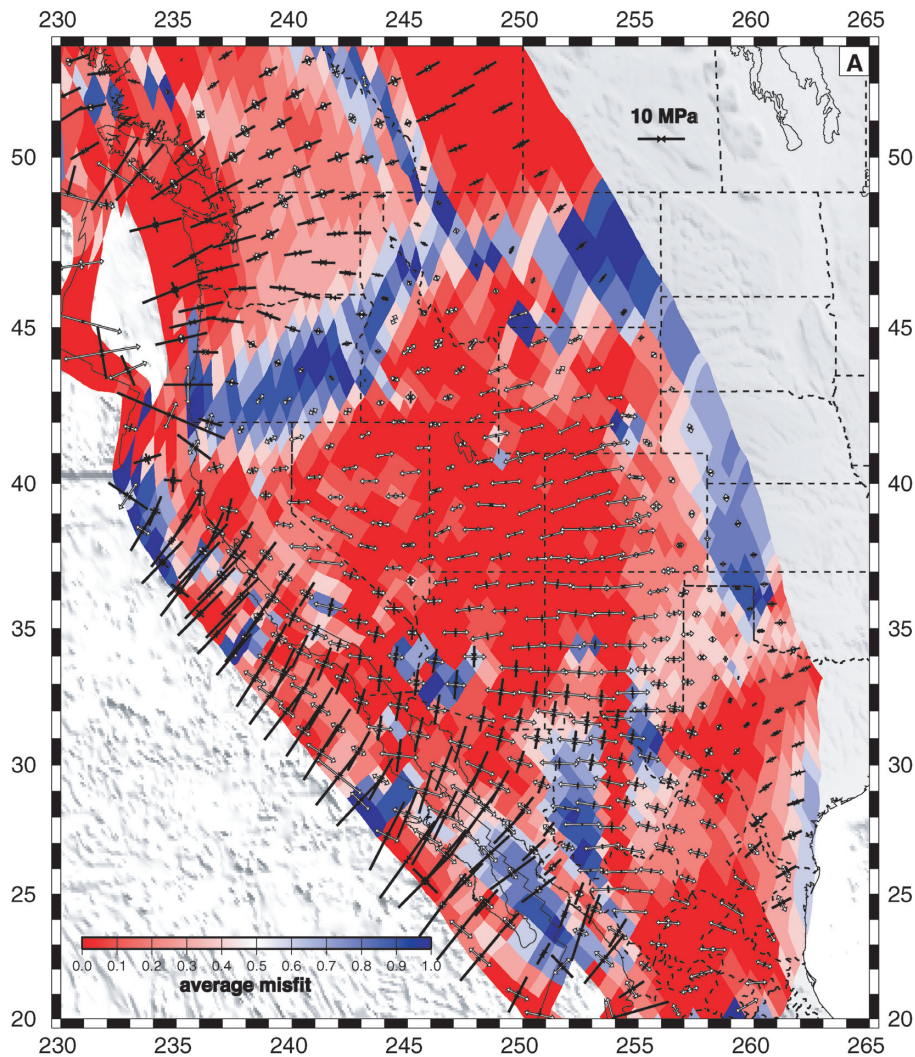


Figure 5. (a) The best-fitting total vertically averaged deviatoric stress field for the western United States portion of the grid for the Airy case. Open arrows represent tensional principal axes of deviatoric stress, closed arrows represent compressional principal axes of deviatoric stress. The misfit function (eq. 21) between deviatoric stress and the strain rate is plotted in the background (see also Table 1 for misfit results by region). (b) Same as shown in (a) but for the Alaska/Canadian Rockies portion of the grid. (c) Same as shown in (a) but for GPE estimates determined from the CRUST2.0 model. (d) Same as shown in (c) but for the Alaska/Canadian Rockies portion of the grid.

where a value of zero misfit for a given area is a perfect match of the relative magnitudes and directions of principal axes of deviatoric stress with the relative magnitudes and directions of principal axes of the strain rate field. A misfit value of 1.0 indicates a complete misfit between the two tensor fields. The average correlation, C , between the unit tensors of the deviatoric stress field and the strain rate field from the kinematic solution, defined as

$$C = \frac{\mathbf{e} \cdot \boldsymbol{\tau}}{ET}, \quad (22)$$

is also provided for each solution in Table 1.

The total deviatoric stress field from the Airy case plus boundary conditions and the CRUST2.0 case plus boundary conditions yield average misfits of 0.24 and 0.25, respectively, for the entire plate boundary zone (Table 1). The regions in Table 1 (shown in Fig. 1) group areas of similar tectonic style and strain rate. Vertically averaged deviatoric stresses within regions 5 and 6 (the Pacific Northwest region) fit the stress indicators for the Airy solution better than the CRUST2.0 case for those two regions (Table 1). On the other hand, the CRUST2.0 model provides a better match to region 9 (the western Great Basin, eastern California Shear Zone, and northern Basin and Range within Oregon) than does the Airy solution (Table 1). Both solutions provide E–W tensional deviatoric stresses across the Great Basin of Nevada and Utah, with deviatoric tensional stress magnitudes there of 3–7 MPa and 5–10 MPa for the Airy and CRUST2.0 cases, respectively. Additionally, both the solutions yield deviatoric stress field estimates that are a close match to the style of deformation along the Wasatch Fault at the eastern edge of the Great Basin (region 10, Table 1). The Airy solution yields low deviatoric stresses east of the Rockies (>1 MPa), whereas the CRUST2.0 solution yields large compressional deviatoric stresses there of 5–12 MPa.

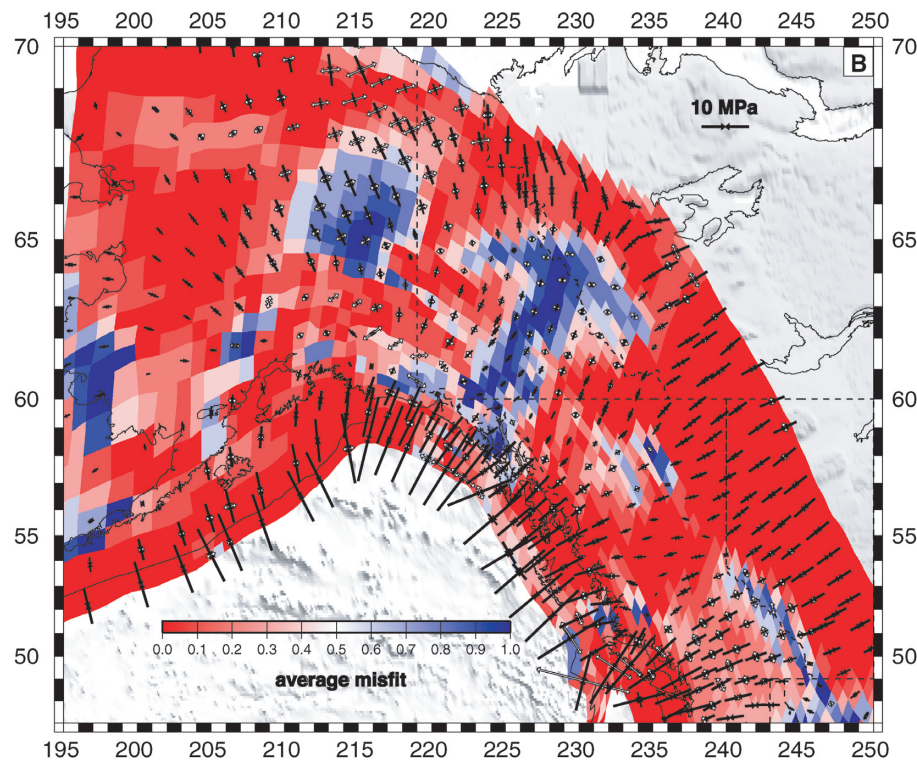


Figure 5. (Continued.)

South of the Big Bend of the San Andreas fault both solutions provide compressional deviatoric stresses that are close to 45° from the strike of the fault with magnitudes of 5 MPa. In the Airy solution, compressional deviatoric stresses of 5–10 MPa are oriented 70° – 80° from the strike of the San Andreas fault north of the Big Bend and along the Big Bend, consistent with borehole stress indicators (Zoback 1989; Zoback & Zoback 1991; Townend & Zoback 2004). In contrast, the CRUST2.0 solution yields nearly pure strike-slip style deviatoric stresses there, with principal axes of compression of 5 MPa oriented at 50° – 60° from the strike of the San Andreas fault. Overall there is good agreement with the previous results of Richardson & Reding (1991) who estimated deviatoric stresses on a coarser grid by matching World Stress Map data. A qualitative comparison of the total deviatoric stress field solution with World Stress Map observations (Zoback & Zoback 1980; Zoback 1989; Zoback & Zoback 1991) provides good agreement with predicted and observed style of deformation (compression normal to the margin to the west, compression normal to the topographic front in the central US and Canada, strike-slip faulting along the San Andreas fault and normal faulting in the Basin and Range). The direction of maximum compressive deviatoric stress produced in the CRUST2.0 model is consistent with the large number of World Stress Map observations in the Canadian Rockies and along the eastern portion of our grid. Interestingly, the direction of the maximum compressive stress produced in the Airy case is in best agreement with the World Stress Map observations along the western margin of North America.

In general, areas of significant misfit appear to be associated with regions with either low strain rates (e.g. Great Plains of United States) or within regions affected by the elastic locking along the Juan de Fuca plate (Figs 5a and c). The region of central and southern Oregon State, for example, provides a poor fit to the stress field indicators. There the deviatoric stress field predicts NE–SW oriented extension (Figs 5a and c) whereas stress field indicators involve primarily N–S compression (Fig. 2c). Another problem region for both solutions is along the Sierra Madre of Mexico, where the total deviatoric stress field predicts predominant E–W oriented extension (Figs 5a and c) but the stress field indicators from the strain rate solution predict NE–SW oriented compression of order 1 nanostrain per year. It is noteworthy to mention that within such low strain rate regions the orientation and relative magnitudes of the principal axes of the strain rate tensor are poorly defined. Therefore, until a more reliable long-term strain rate tensor field can be obtained, the misfits of the deviatoric stress field with the stress field indicators within the low strain rate regions should be interpreted with caution.

Vertically averaged deviatoric stresses for both solutions within Alaska and Western Canada (Figs 5b and d) show compression of order 10–15 MPa along the subduction trench and along the Queen Charlotte Fault zone. Both solutions predict deviatoric tension along the higher elevations within Alaska and mixed strike-slip and thrust elsewhere throughout Alaska (Figs 5b and d). Surprisingly the deviatoric stresses could not match the strike-slip style stress indicators along the Queen Charlotte fault zone (Fig. 2d), but instead predict compressional deviatoric stresses roughly orthogonal to the fault strike. The misfits in this region could be related to stress/strain anisotropic behaviour in this region. Although we have not excluded the directions and styles of stress indicators along the Fairweather fault zone, as we have done for the San Andreas section of the plate boundary zone, such exclusion would not alter the result of deviatoric compressional stress roughly

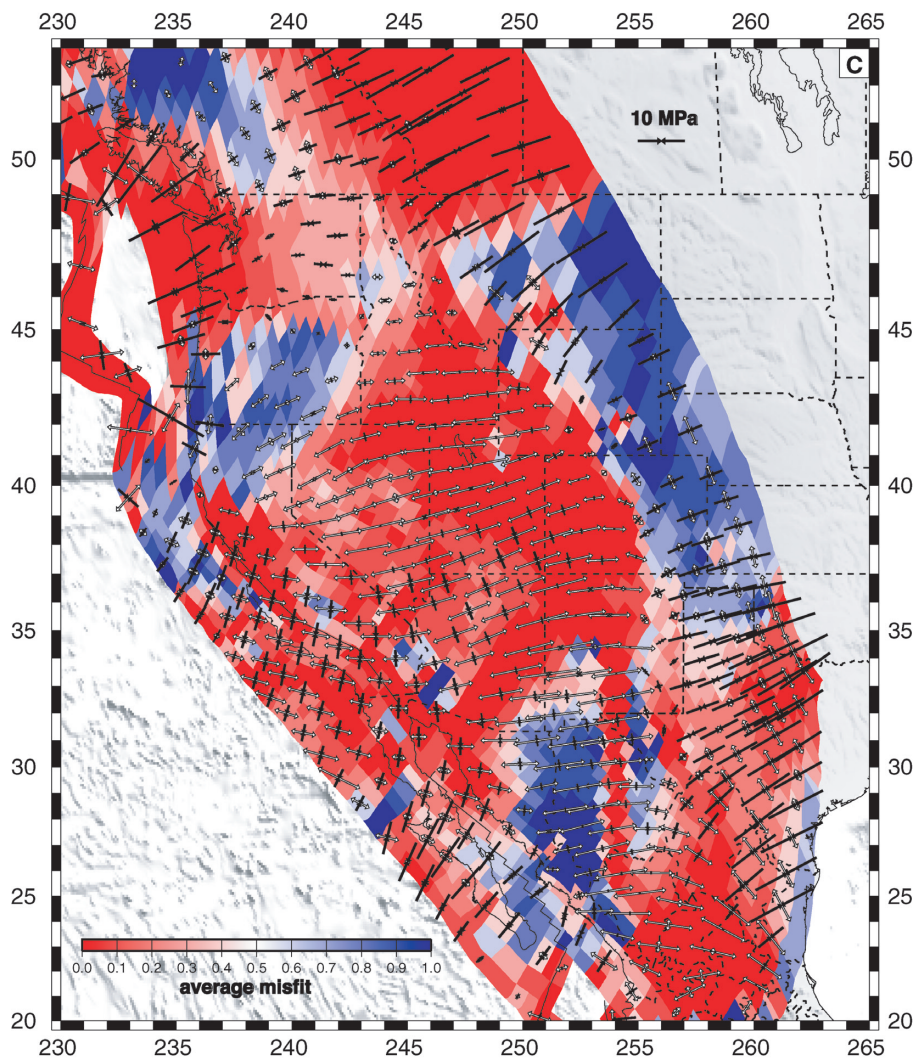


Figure 5. (Continued.)

orthogonal to the strike of the Fairweather fault. Rather, exclusion of stress indicators there would remove all information to indicate the strike-slip nature of this portion of the plate boundary zone. Therefore, the result along the Fairweather fault is likely dictated by the need to match stress indicators throughout the much larger region to the east of the Fairweather fault zone, which are dominantly compressional.

3.5 The deviatoric stress field associated with basal tractions

The modelling in Sections 3.2–3.4 has thus far ignored any contributions from the tractions associated with the convecting mantle below the lithosphere ($f_{2\alpha}$ terms set to zero). Therefore, we now use the results from large-scale 3-D mantle flow models to calculate deviatoric stress associated with tractions at the base of the lithosphere. We solve equations in (13) (or (17) with $f_{1\alpha}$ terms now set to zero) again by minimizing the J functional in (18).

The input basal traction field (Fig. 6) is generated from a large-scale 3-D mantle flow calculation for the entire globe (Wen & Anderson 1997a), for an upper mantle with laterally uniform viscosity (1×10^{21} Pa s). The traction field in Fig. 6 is similar to that presented by Lithgow-Bertelloni & Guynn (2004). The density structure in the upper mantle was inferred by adjusting the relative weights of density anomalies of subducted slabs (Wen & Anderson 1995) and residual tomography (Wen & Anderson 1997b). The density structure in the lower mantle was derived from the tomography model of Su *et al.* (1994). The detailed information for the density model and the velocity-density scaling were presented in Wen & Anderson (1997c). Although lateral viscosity variations within the asthenosphere are no doubt important and contribute to toroidal components of the basal shear field, we use only a poloidal mantle solution (isoviscous). The toroidal portion of the basal tractions are implicitly included within the stress field boundary conditions (Fig. 4) everywhere up to the boundary of our grid; potential toroidal components of the tractions associated with coupled mantle circulation are only absent within the interior of the grid. The importance of weak plate boundary zones on the mantle flow field and plate boundary zone deformation field have been noted before (e.g. see

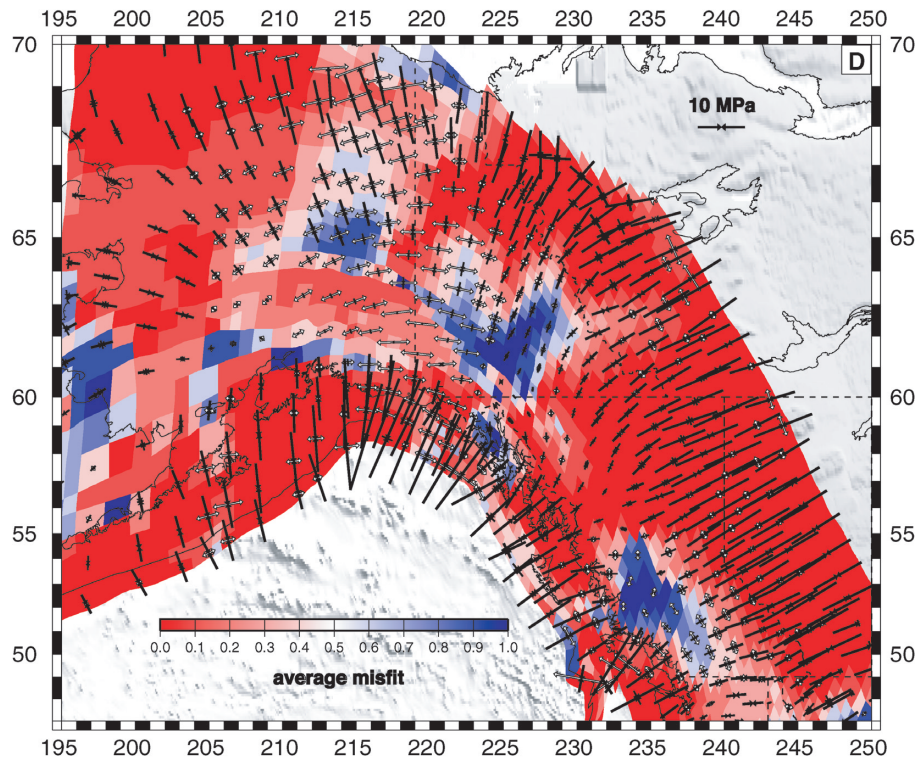


Figure 5. (Continued.)

Zhong & Gurnis 1996; Choi & Gurnis 2003). We suspect that the weak plate boundary zone along the transform-dominated section of North America plays an important role in generating a toroidal component of the traction field, and that the influence of this toroidal component of the traction field is accounted for in our stress field boundary conditions (which are dominated by a pervasive shear signature, Fig. 4). The poloidal portion of the traction field is present in our traction solution and is associated with the large-scale density buoyancy driven flow that results from the sinking Farallon slab (Bunge & Grand 2000; Steinberger & OConnell 2000; Humphreys *et al.* 2003; Lithgow-Bertelloni & Gynn 2004). Because we are using an isoviscous upper mantle, we input the poloidal portion of the basal traction that is expressed as $\Phi_{xx} = \Phi_{yy} = -\frac{1}{3}Z_4^m Y_{lm}$, where Z_4^m and Y_{lm} are the poloidal coefficients and associated Legendre polynomials, respectively, from the flow calculations determined out to degree and order 30 (Wen & Anderson 1997a). Stresses associated with basal tractions are calculated globally, but only those stresses contained within our grid are used in the inversion (Fig. 7). With an independent estimation of the stress field associated with basal tractions, we then solve for a stress field boundary condition and total deviatoric stress field following the method described in Section 3.3 by minimizing the objective function (eq. 20), only now we define the total stress field as

$$\tau = \tau_0 + b\tau_b + \sum_{j=1}^{nseg} \sum_{i=1}^3 a_{ij}\tau_{ij}, \quad (23)$$

where τ_b is the deviatoric stress field associated with global solution of basal tractions (Fig. 7), and b is the scaling factor that multiplies the stresses associated with basal tractions and is determined in the inversion.

We find there is a trade-off between the basal scaling factor, b , and the stress field boundary conditions. Because of this trade-off, we are unable to discriminate the exact level of tractions acting on the base of the lithosphere in this regional model alone. The total deviatoric stress field is invariant to the level of basal tractions included in the inversion; what changes are the stress field boundary conditions. With higher scaling factors for basal tractions the boundary condition solutions are effectively canceling out the larger deviatoric tensional stresses, associated with the basal tractions (Fig. 7), with generally NW-SE compression (Supplementary Figs S2 and S3). This may indicate the need for low basal tractions beneath the plate boundary zone. Furthermore, the sum of the basal traction and stress field boundary conditions is constant for all scaling factors and is identical to the deviatoric stress field with no basal tractions (e.g. Fig. 4 and Supplementary Figs S21 and S31). Thus, we are confident that the total deviatoric stress field (GPE solution + scaled basal traction solution + boundary condition) provides a robust global minimum of misfit with the stress field indicators. That is, the sum of boundary conditions plus scaled basal tractions provides a robust estimate of the magnitudes, styles, and directions of principal axes of deviatoric stress.

Table 1. The model fit with the stress field indicators for different regions shown in Fig. 1.

Region of interest	Number of areas	Total regional area ^a	Average strain magnitude ^b	Total misfit ^c	Average misfit ^d	Average correlation between unit tensors ^e	Average misfit between unit tensors ^f
GPE estimated assuming the lithosphere is in Airy isostatic balance							
All	3574	0.29	54.5	8.3e5	2.8e6	0.53	0.24
1	66	6.5e-3	2.3	3.6e3	5.6e5	0.81	0.10
2	365	3.3e-2	111.7	5.7e4	1.7e6	0.52	0.24
3	325	1.7e-2	6.6	1.5e4	8.9e5	0.64	0.18
4	118	7.3e-3	111.5	2.8e4	3.9e6	0.57	0.22
5	71	6.4e-3	55.5	3.5e4	5.4e6	0.43	0.29
6	116	7.7e-3	5.0	1.7e4	2.2e6	0.62	0.19
7	257	2.8e-2	216.7	1.7e5	6.0e6	0.46	0.27
8	141	1.2e-2	11.6	3.8e4	3.1e6	0.43	0.28
9	146	1.2e-2	4.0	2.0e4	1.6e6	0.47	0.26
10	30	2.0e-3	8.5	4.6e2	2.2e5	0.94	0.03
11	162	2.0e-2	41.5	2.3e4	1.2e6	0.56	0.22
12	511	4.1e-2	1.8	1.2e5	2.9e6	0.54	0.23
GPE estimates made using the CRUST2.0 (Mooney <i>et al.</i> 1998) crustal thickness model							
All	3574	0.29	54.5	1.2e6	4.0e6	0.51	0.25
1	66	6.5e-3	2.3	5.6e3	1.0e6	0.88	0.06
2	365	3.3e-2	111.7	1.0e5	3.1e6	0.47	0.26
3	325	1.7e-2	6.6	1.5e4	8.7e5	0.87	0.06
4	118	7.3e-3	111.5	2.8e4	3.9e6	0.57	0.22
5	71	6.4e-3	55.5	3.4e4	5.4e6	0.25	0.38
6	116	7.7e-3	5.0	1.9e4	2.5e6	0.42	0.29
7	257	2.8e-2	216.7	9.5e4	3.4e6	0.47	0.26
8	141	1.2e-2	11.6	7.4e4	6.1e6	0.37	0.31
9	146	1.2e-2	4.0	3.7e4	3.2e6	0.60	0.20
10	30	2.1e-3	8.5	1.1e3	5.3e5	0.96	0.02
11	162	2.0e-2	41.5	1.0e5	5.3e6	0.46	0.27
12	511	4.1e-2	1.8	2.5e5	6.1e6	0.39	0.31
GPE estimated assuming the lithosphere is in Airy isostatic balance using a 'long-term' kinematic solution ^g							
All	3574	0.29	54.5	7.7e5	2.7e6	0.58	0.21
1	66	6.5e-3	2.3	3.6e3	5.6e5	0.82	0.09
2	365	3.3e-2	111.7	5.5e4	1.6e6	0.53	0.23
3	325	1.7e-2	6.6	1.6e4	9.3e5	0.58	0.21
4	118	7.3e-3	111.5	2.4e4	3.4e6	0.60	0.20
5	71	6.4e-3	55.5	2.2e4	3.4e6	0.48	0.26
6	116	7.7e-3	5.0	8.8e3	1.1e6	0.65	0.17
7	257	2.8e-2	217.7	1.6e5	5.8e6	0.46	0.27
8	141	1.2e-2	11.6	3.4e4	2.7e6	0.50	0.25
9	146	1.2e-2	4.0	7.1e3	6.2e5	0.87	0.07
10	30	2.0e-3	8.5	961.7	4.7e5	0.91	0.05
11	162	2.0e-2	41.5	1.7e4	8.7e5	0.72	0.14
12	511	4.1e-2	1.8	1.2e5	3.0e6	0.61	0.20

3.6 A revised long-term estimate of the deviatoric stress field

In Section 2, we have referred to problems associated with elastic signal of the locked Juan de Fuca subduction zone. Therefore, we investigate a final dynamic solution using a revised kinematic model in which we exclude GPS observations north of the Mendicino Triple Junction in order to avoid possible elastic effects related to the locked Juan de Fuca, Gorda and Explorer plates. However, GPS observations within Yellowstone region, as well as within Alaska are still used in the inversion. We also constrain the Sierra Nevada block and the Cascadia forearc to be more rigid than surrounding regions (e.g. Dixon *et al.* 2000; Whitehouse *et al.* 2005) by decreasing the variances of the rates of strain in the kinematic solution an order of magnitude within those regions, which has the influence of damping the model strain rates within those regions (Beavan & Haines 2001). Velocity boundary conditions and fault data remain the same as in previous models. As a consequence of removing the GPS data within the Pacific Northwest region, as well as adding the constraint of a rigid Cascadia forearc, all Juan de Fuca—North American Plate relative motion is accommodated at the Juan de Fuca trench (Fig. 8a). Strain rates are thus low within the Cascadia forearc where principal axes of compressional strain rate are oriented N–S. East of the Cascade Range, principal axes of strain are oriented NNE. Finally, the relative motions of the Cascadia forearc in this model are similar to that proposed by Wells *et al.* (1998) (see Fig. 8b).

The stress field boundary condition solutions (Fig. 9) determined using the long-term kinematic estimates, are similar to those determined in Section 3.2 and shown in Fig. 4. Overall, the long-term total deviatoric stress fields, for both the Airy and CRUST2.0 cases (Fig. 10), yield an improved fit with the deformation indicators with total average misfits of 0.21 and 0.22, respectively (Table 1). The primary improvement

Table 1. (Continued.)

Region of interest	Number of areas	Total regional area ^a	Average strain magnitude ^b	Total misfit ^c	Average misfit ^d	Average correlation between unit tensors ^e	Average misfit between unit tensors ^f
GPE estimates made using the CRUST2.0 (Mooney <i>et al.</i> 1998) using a 'long-term' kinematic solution ^g							
All	3574	0.29	54.5	1.1e6	3.7e6	0.55	0.22
1	66	6.5e-3	2.3	6.3e3	9.6e5	0.88	0.06
2	365	3.3e-2	111.7	1.0e5	3.0e6	0.48	0.26
3	325	1.7e-2	6.6	1.7e4	9.9e5	0.82	0.09
4	118	7.3e-3	111.5	2.2e4	3.1e6	0.59	0.21
5	71	6.4e-3	55.5	2.8e4	4.3e6	0.27	0.37
6	116	7.7e-3	5.0	2.3e4	3.0e6	0.34	0.33
7	257	2.8e-2	216.7	8.7e4	3.1e6	0.54	0.23
8	141	1.2e-2	11.6	6.1e4	5.0e6	0.49	0.26
9	146	1.2e-2	4.0	2.4e4	2.1e6	0.82	0.09
10	30	2.0e-3	8.5	1.5e3	7.3e5	0.96	0.02
11	162	2.0e-2	41.5	6.9e4	3.5e6	0.61	0.19
12	511	4.1e-2	1.8	2.5e5	6.3e6	0.46	0.27

^aArea normalized by the square of the radius of the Earth.

^bThe average strain rate magnitude is defined as $\sqrt{\frac{\sum_{\text{areas}} |\dot{E}^2| \Delta S}{\sum_{\text{areas}} \Delta S}}$.

Strain rate units are $\times 10^{-9}$ yr⁻¹.

^cThe total misfit to the functional as defined in eq. (20), $\sum_{\text{areas}} (T - \frac{e \cdot \tau}{E}) \Delta S$, where

$$E = \sqrt{\dot{\epsilon}_{xx}^2 + \dot{\epsilon}_{yy}^2 + \dot{\epsilon}_{zz}^2 + \dot{\epsilon}_{xy}^2 + \dot{\epsilon}_{yx}^2} = \sqrt{2\dot{\epsilon}_{xx}^2 + 2\dot{\epsilon}_{xx}\dot{\epsilon}_{yy} + 2\dot{\epsilon}_{yy}^2 + 2\dot{\epsilon}_{xy}^2},$$

$$T = \sqrt{\tau_{xx}^2 + \tau_{yy}^2 + \tau_{zz}^2 + \tau_{xy}^2 + \tau_{yx}^2} = \sqrt{2\tau_{xx}^2 + 2\tau_{xx}\tau_{yy} + 2\tau_{yy}^2 + 2\tau_{xy}^2},$$

$$e \cdot \tau = \dot{\epsilon}_{xx}\tau_{xx} + \dot{\epsilon}_{yy}\tau_{yy} + \dot{\epsilon}_{zz}\tau_{zz} + \dot{\epsilon}_{xy}\tau_{xy} + \dot{\epsilon}_{yx}\tau_{yx} = 2\dot{\epsilon}_{xx}\tau_{xx} + \dot{\epsilon}_{xx}\tau_{yy} + \dot{\epsilon}_{yy}\tau_{xx} + 2\dot{\epsilon}_{yy}\tau_{yy} + 2\dot{\epsilon}_{xy}\tau_{xy},$$

and ΔS is the local area. Stress units are MPa.

^dAverage misfit to the functional is defined as $\frac{\sum_{\text{areas}} (T - \frac{e \cdot \tau}{E}) \Delta S}{\sum_{\text{areas}} \Delta S}$.

^eThe average correlation between the unit tensors is defined as $\frac{\sum_{\text{areas}} (\frac{e \cdot \tau}{ET}) \Delta S}{\sum_{\text{areas}} \Delta S}$.

^fThe average misfit between unit tensors is defined as $\frac{\sum_{\text{areas}} 0.5 * (1 - \frac{e \cdot \tau}{ET}) \Delta S}{\sum_{\text{areas}} \Delta S}$.

^gLong-term kinematic solution refers to the solution in which GPS vectors in regions that are affected by the subduction-zone coupling have been omitted from the calculation.

to the dynamic model, which results from using a revised estimate of the kinematic solution as a proxy for the long-term deformation field, provides a dramatically better fit within regions 9 and 11 (western Great Basin, eastern California shear zone and northern Basin and Range within southern Oregon) (Fig. 10; Table 1). There is also a slightly improved fit within region 11 (Table 1). Finally, within the northern Basin and Range, within eastcentral and southern Oregon, the long-term dynamic model predicts E–W extension. We conclude that the longer-term dynamics are more in accord with the kinematic solution that has no elastic signal from the locked Juan de Fuca—North American Plate (Fig. 8b), and this solution is our preferred long-term estimate for the dynamics of western North America.

4 STRESS MAGNITUDES AND IMPLICATIONS FOR STRENGTH PROFILES

Although we have solved for deviatoric stresses as a vertical average, we next make inferences about the possible depth dependence of deviatoric stress. This is a non-unique problem, but the magnitudes of our vertically averaged deviatoric stresses are robust and can place bounds on possible strength profile models. We investigate two end-member strength profile models (Fig. 11). In case A in Fig. 11, the crust is stronger than the mantle (Kohlstedt *et al.* 1995), as might be the case for a wet olivine mantle rheology. In case A the upper mantle makes only a small contribution to the total vertically averaged deviatoric stress magnitude. In case B of Fig. 11 the crust is weaker than the mantle (Molnar 1992), as might be the case for a dry mantle rheology. For either of these cases, the area under each strength profile curve must be equal to the depth integral of deviatoric stress, or equivalently L times our vertical average of deviatoric stress (see Flesch *et al.* 2001, for details). Because the area under each strength profile must equate to our vertically averaged deviatoric stress estimates, the magnitudes of the strength profiles are calibrated by the shape of the strength curves. Assuming a vertically averaged stress of 7.5 MPa, roughly the value for the San Andreas fault region and the Basin and Range (Figs 5 and 10), case A predicts deviatoric stress levels of 50–110 MPa at 5–12 km depths, consistent with extrapolations of bore hole measurements (Brudy *et al.* 1997), and laboratory and theoretical friction experiments (Sibson 1982; Kohlstedt *et al.* 1995). Case B predicts deviatoric stress levels of 6.5–10 MPa at 5–12 km depth, roughly that of earthquake stress drops for intraplate earthquakes (Kanamori & Anderson 1975). We would argue that for our vertical averages to be consistent with

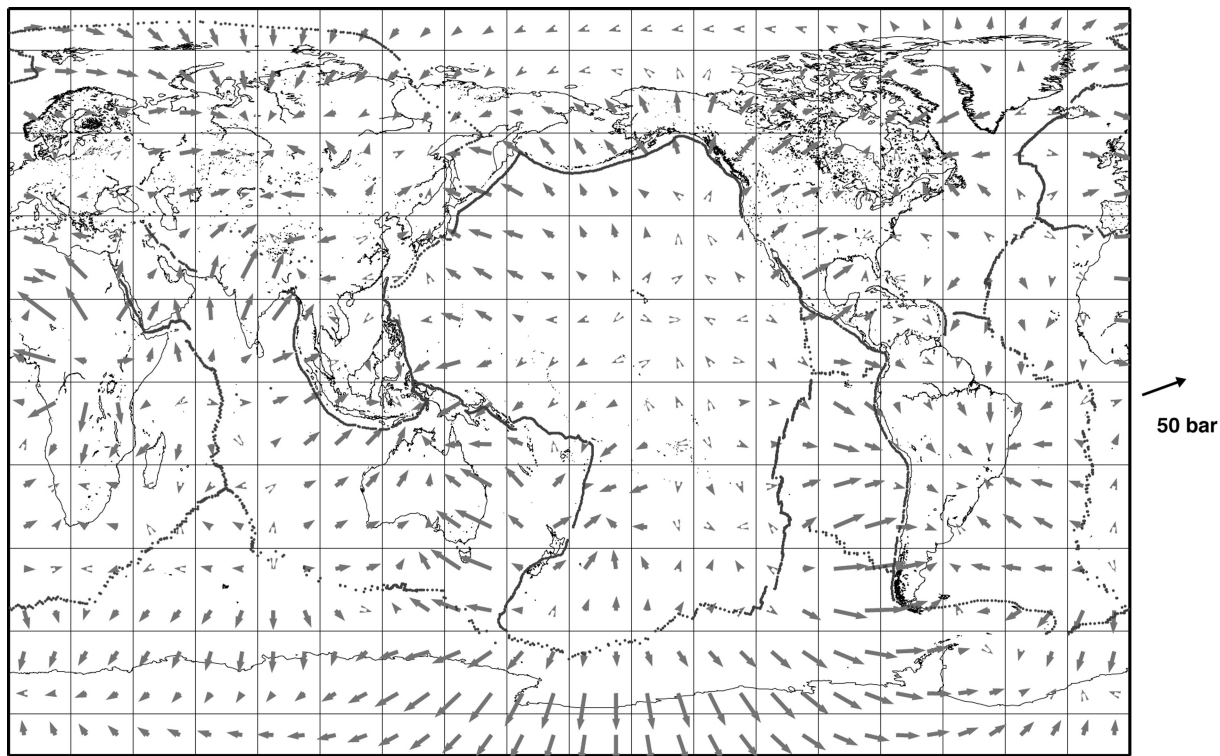


Figure 6. Basal tractions generated by laterally uniform viscosity model with upper mantle viscosity of 1×10^{21} Pa s. Density model is inferred from a tomography model from Su *et al.* (1994) using scaling relationships from Wen & Anderson (1997a) and subduction history from Wen & Anderson (1995). Flow field is poloidal because of uniform mantle viscosity.

observed borehole and laboratory measurements that a significant portion of the strength of the lithosphere be contained within the upper seismogenic zone, (case A) for the deforming western United States. If there is a weak decoupling layer between the seismogenic crust and the upper mantle, then our results are still consistent with a strong seismogenic upper crust, but in such a case we are unable to infer any information about the strength of the upper mantle.

5 DISCUSSION AND CONCLUSIONS

We have quantified the absolute magnitudes and directions of vertically averaged deviatoric stresses within the western North American Plate boundary zone. The method enables us to directly solve for the vertically averaged deviatoric stress, given estimates of the spatial distribution of effective body forces ($1/L$ times gravitational potential energy per unit area values and applied basal tractions). We have shown that boundary conditions plus scaled basal tractions provide a robust best-fitting deviatoric stress field for all values of basal scaling. This result indicates there is one unique deviatoric stress field solution (unique in magnitude and unique in style and direction) that when added to the solution associated with GPE distributions provides a global minimum in misfit with the stress field indicators. However, there is insufficient information in the regional GPE field and in the spatial variation in deformation indicators to resolve the degree of coupling with mantle flow beneath western NA. The coupling can likely be quantified with global models (e.g. Ghosh *et al.* 2005, 2006). We have argued that the integrated effect of global lithospheric GPE distributions and global traction distributions defines the boundary condition along the plate boundary zone. The advantage of global modelling is that full global density buoyancy distributions, along with lateral and vertical variations in viscosity, are explicitly put into the model in order to define a best-fitting solution globally. With such a modelling procedure the degree of coupling beneath any region of interest can then likely be more directly inferred.

The deviatoric stress field associated with GPE variations calibrates the magnitudes of the total deviatoric stresses acting within the lithosphere. Thus, the accuracy of our solution is dependent upon the accuracy of the GPE estimates. For this reason, we have inferred GPE values from two different sources.

The CRUST2.0 solution is most likely a more accurate representation of the GPE distributions of the lithosphere, since it is constrained with seismic observations (e.g. Mooney *et al.* 1998). The relative pattern of differences in GPE that result from the Airy model are only likely to be representative of actual GPE variations if there is a decoupling of the upper seismogenic portion of the continental crust from deeper density buoyancies within the lower crust and upper most mantle lithosphere. Given that the Airy solution and the CRUST2.0 solution yield similar matches to the stress field indicators (Table 1), we are not able to discriminate between models of complete crustal decoupling, or complete coupling.

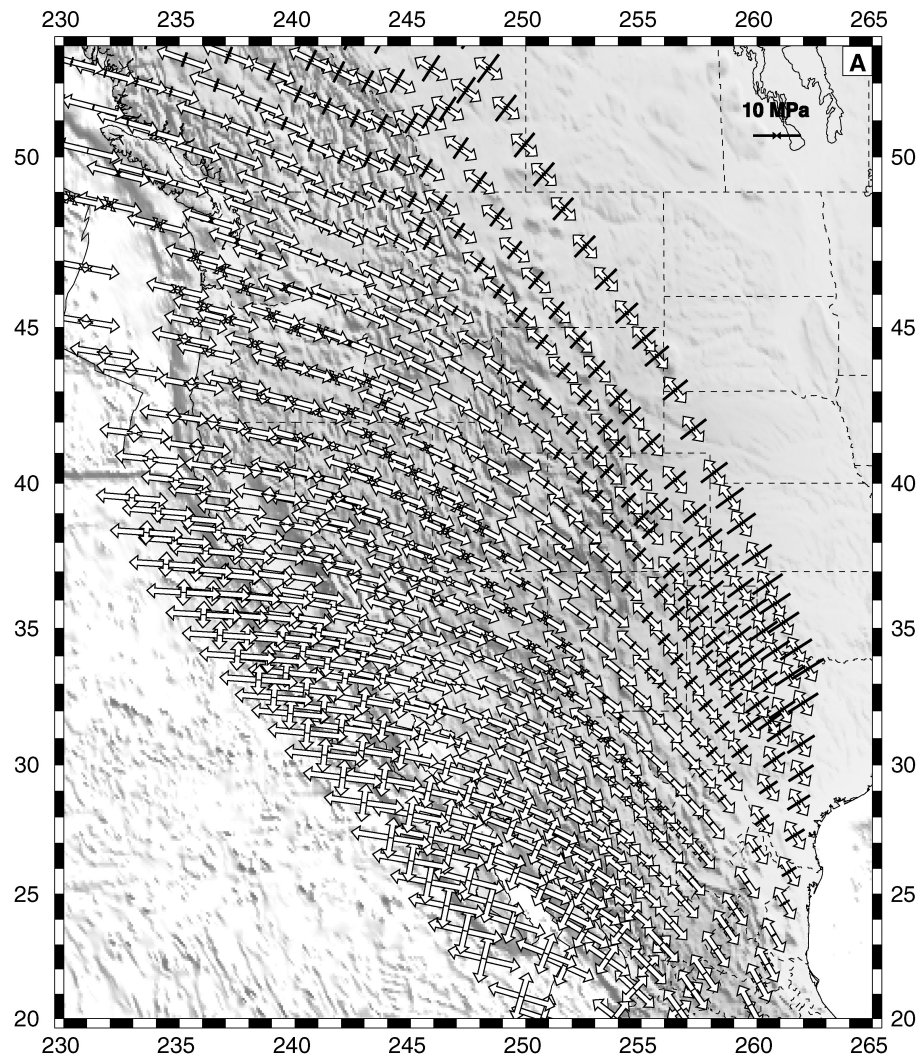


Figure 7. (a) The vertically averaged deviatoric stress field associated with the basal traction field shown in Fig. 6. Open white arrows denote tensional principal axes of deviatoric stress, closed black arrows denote compressional principal axes of deviatoric stress. The stress field was determined globally but is only plotted within the region of interest. (b) Same as shown in (a) but for the Alaska/Canadian Rockies portion of the grid.

What is significant from these results is that two different estimates of GPE distributions yield, when combined with stress boundary conditions, similar quantitative matches to the stress field indicators and similar values for vertically averaged deviatoric stress. A global treatment will not change this result. Although the vertically averaged deviatoric stresses calculated from the CRUST2.0 model are generally larger by as much as a factor of two from those estimated from the Airy case, a robust conclusion is that, for western North America, deviatoric stresses associated with GPE differences provide about 50 per cent of the driving force (Fig. 3) and stress boundary conditions provide the remaining 50 per cent of stress magnitudes (Figs 4 and 9) in the total vertically averaged deviatoric stress field solution (Figs 5 and 10). The stress field boundary conditions represent the total influence of tractions and lithospheric buoyancy effects everywhere outside the region modelled, as well as an approximation of the influence of tractions inside the region modelled. These stress field boundary conditions appear to be in accord with that associated with shear between the Pacific and North American Plates and convergence of the Juan de Fuca plate with North America. Force-balance dictates that such interactions will have a long-wavelength character that will span the width of the plate boundary zone, as observed in (Figs 4a, c, 9a and c). Our preferred estimate of the long-term dynamics (Fig. 10) results from a solution where no GPS were used within the Pacific Northwest in order to remove the elastic effects of a locked subduction zone at the Juan de Fuca trench (Supplementary Figs S4a and b). An important refinement of the long-term dynamics can only be obtained with an accurate estimate of the long-term kinematics. This requires a more complete data set of rates and distributions of quaternary faulting throughout the plate boundary zone.

The magnitudes of vertically averaged deviatoric stresses (within a 100 km thickness) are of order 10 MPa. These magnitudes of deviatoric stresses are on the low end of what has been obtained for vertical averages of deviatoric stress within the lithosphere and are consistent with the relatively low magnitudes of vertically averaged deviatoric stresses obtained by Richardson (1987), Richardson & Reding (1991) and Richardson & Coblenz (1994). Such low values of vertically averaged deviatoric stress within the lithosphere contrast, for example, with the

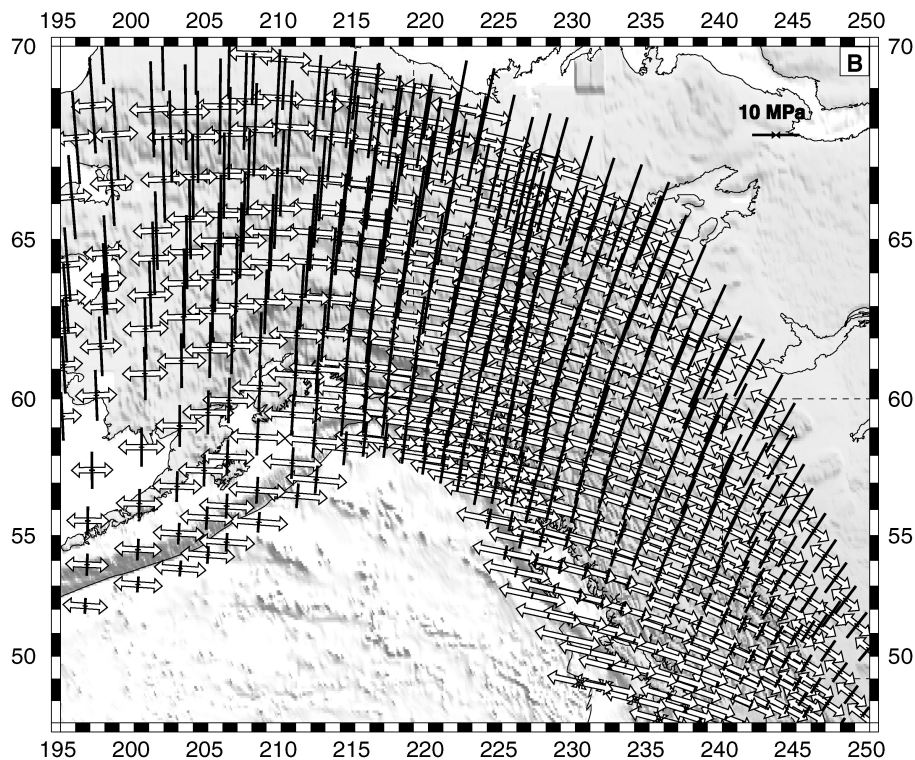


Figure 7. (Continued.)

much higher predictions of vertically averaged deviatoric stress of 100 MPa obtained by Cloetingh & Wortel (1985, 1986) within the Indian Ocean. Our results suggest that the deforming lithosphere within western North America supports vertically averaged deviatoric stresses that are an order of magnitude lower than this. We have shown that if Byerlee friction holds for the seismogenic portion of the lithosphere then these stresses suggest that the bulk of the lithospheric strength lies within the brittle seismogenic portion of the lithosphere. Accordingly, the vertically averaged deviatoric stresses we have calculated suggest that the lower crust and upper mantle within the plate boundary zone are much weaker than the seismogenic crust and support much lower deviatoric stresses. For such a model the deviatoric stresses peak at values of order 100 MPa at the base of the seismogenic zone. If, however, the crust and mantle are completely decoupled, then our results argue for a strong controlling upper crustal layer, but cannot provide any information on the strength of the mantle. Finally, our vertically averaged stress magnitudes, and the implications for a strong seismogenic crust and weak lower crust and upper mantle, are in accord with inferences made by Jackson (2002) based on relocation of earthquake focal depths and elastic thicknesses. Moreover, the inferences of a weaker lower crust and upper mantle are in accord with shoreline and post-seismic relaxation times that suggest low mantle viscosities of order 10^{18} – 10^{19} Pa s (Bills *et al.* 1994; Deng *et al.* 1998; Pollitz *et al.* 1998) and acting stresses within the weak zone below the seismogenic layer that are of the order of the stress changes (a few tenths of a MPa) produced in earthquakes (Montesi 2004).

ACKNOWLEDGMENTS

We thank David Coblenz, Gene Humphreys and editor John Beavan for helpful reviews of this manuscript. We thank Corné Kreemer for help with the GPS data. We are grateful to Rick Bennett for providing GPS data. This work made use of the UNAVCO Facility supported by the National Science Foundation under NSF Cooperative Agreement No. EAR-031760. Maps were prepared using GMT by P. Wessel and W.F. Smith. This work was supported by NSF grants EAR 0001160 and EAR-0215625 to WEH, NSF EAR 0310193 to WEH and LW, and a NASA NIP grant to LW.

REFERENCES

- Antonelis, K., Johnson, D.J., Miller, M.M. & Palmer, R., 1999. GPS determination of current Pacific-North American plate motion, *Geology*, **27**(4), 299–302.
- Atwater, T., 1970. Implications of plate tectonics for the Cenozoic tectonic evolution of western North America, *Bull. Geol. soc. Am.*, **81**, 3513–3536.
- Beavan, J. & Haines, J., 2001. Contemporary horizontal velocity and strain rate fields of the Pacific-Australian plate boundary zone through New Zealand, *J. geophys. Res.*, **106**, 741–770.
- Bennett, R.A., Davis, J.L. & Wernicke, B.P., 1999. Present-day pattern of Cordilleran deformation in the western United States, *Geology*, **27**(4), 371–374.
- Bennett, R.A., Davis, J.L., Normandeau, J.E. & Wernicke, B.P., 2001. Space Geodetic Measurements of Plate Boundary Deformation in the Western U.S Cordillera, Plate Boundary Zones, American Geophysical Union Geophysical Monograph.

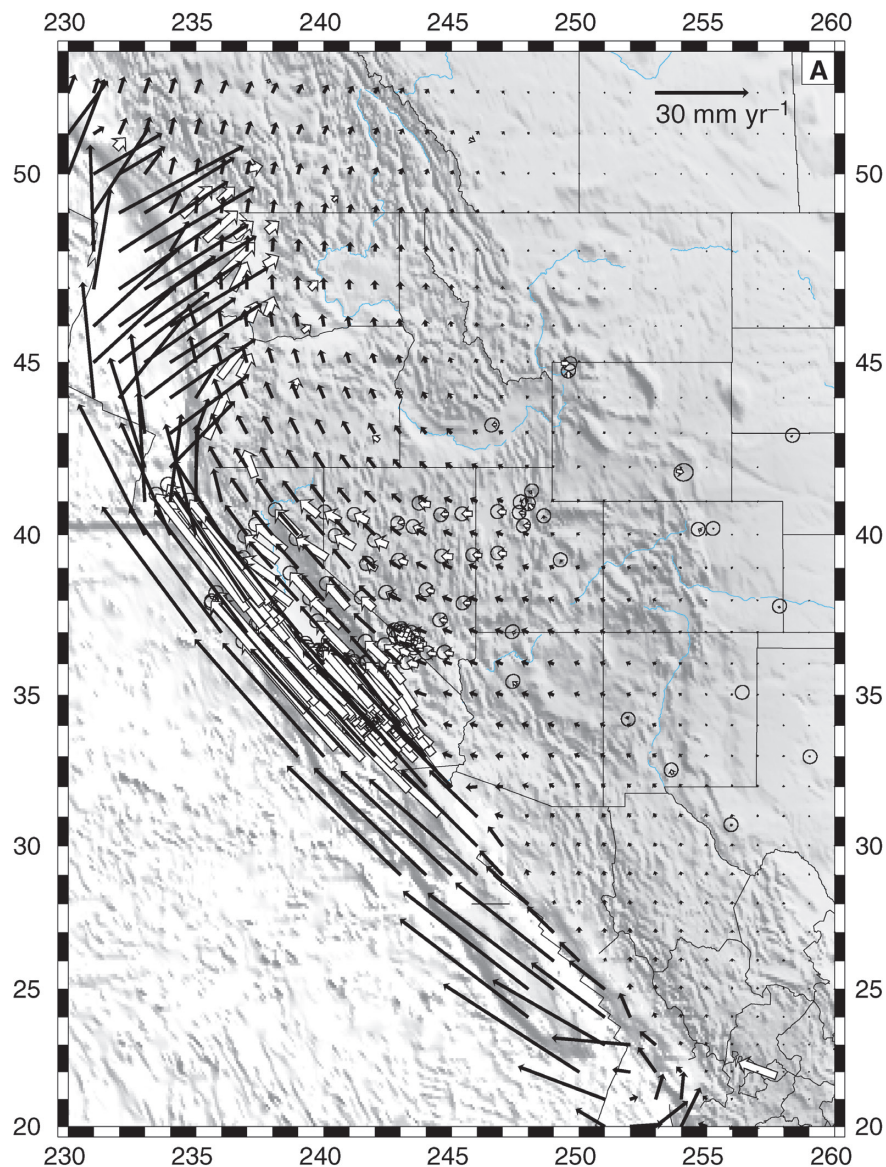


Figure 8. (a) The long-term continuous model velocity field (black vectors) determined without using GPS observations in the Pacific Northwest that contain elastic effects from the subduction of the Juan de Fuca plate. The GPS data from Bennett *et al.* (1999) is also plotted (white vectors), note the disagreement between the long-term solution and GPS data in western Oregon and Washington. (b) The long-term continuous model strain rate field associated with the velocity field shown in Fig. 8(a). Strain rates are plotted as unit tensors and strain rate magnitudes are plotted in the background shaded grid. Open arrows represent extensional strain rates and closed arrows represent compressional strains.

- Bennett, R.A., Wernicke, B.P., Niemi, N.A., Friedrich, A.M. & Davis, J.L., 2003. Contemporary strain rates in the northern Basin and Range province from GPS data, *Tectonics*, **22**(2), 1008, doi:10.11029/2001TC001355.
- Bills, B.G., Currey, D.R. & Marshall, G.A., 1994. Viscosity estimates of the crust upper mantle from patterns of lacustrine shoreline deformation in the eastern Great Basin, *J. geophys. Res.*, **99**, 22,059.
- Bird, P., 1996. Computer simulations of Alaskan neotectonics, *Tectonics*, **15**(2), 225–236.
- Bird, P. & Piper, K., 1980. Plane-Stress Finite-Element Models of Tectonic Flow in Southern-California, *Phys. Earth planet. Inter.*, **21**, 158–175.
- Bohannon, R.G. & Parsons, T., 1995. Tectonic Implications of Post-30 Ma Pacific and North-American Relative Plate Motions, *Geol. Soc. Am. Bull.*, **107**(8), 937–959.
- Brudy, M., Zoback, M.D., Fuchs, K., Rummel, F. & Baumgartner, J., 1997. Estimation of the complete stress tensor to 8 km depth in the KTB scientific drill holes: Implications for crustal strength, *J. Geophys. Res. Solid Earth*, **102**(B8), 18 453–18 475.
- Bunge, H.P. & Grand, S.P., 2000. Mesozoic plate-motion history below the northeast Pacific Ocean from seismic images of the subducted Farallon slab, *Nature*, **405**(6784), 337–340.
- Choi, E.-s. & Gurnis, M., 2003. Deformation in transcurrent and extensional environments with widely spaced weak zones, *Geophys. Res. Lett.*, **30**(2), 1076, doi:10.1029/2002GL016129.
- Cloetingh, S.A.P.L. & Wortel, M.J.R., 1985. Regional stress field in the Indian plate, *Geophys. Res. Lett.*, **12**, 77–80.
- Cloetingh, S.A.P.L. & Wortel, M.J.R., 1986. Stress in the Indo-Australian plate, *Tectonophysics*, **132**, 49–67.
- Dalmayrac, B. & Molnar, P., 1981. Parallel thrust and normal faulting in Peru and constraints on the state of stress, *Earth planet. Sci. Lett.*, **55**(3), 473–481.
- Deng, J.S., Gurnis, M. & Kanamori, H., 1998. Viscoelastic flow in the lower crust after the 1992 Landers, California, earthquake, *Science*, **282**, 1689.
- DeMets, C., 1995. A reappraisal of seafloor spreading lineations in the Gulf of California: Implications for the transfer of Baja California to the Pacific

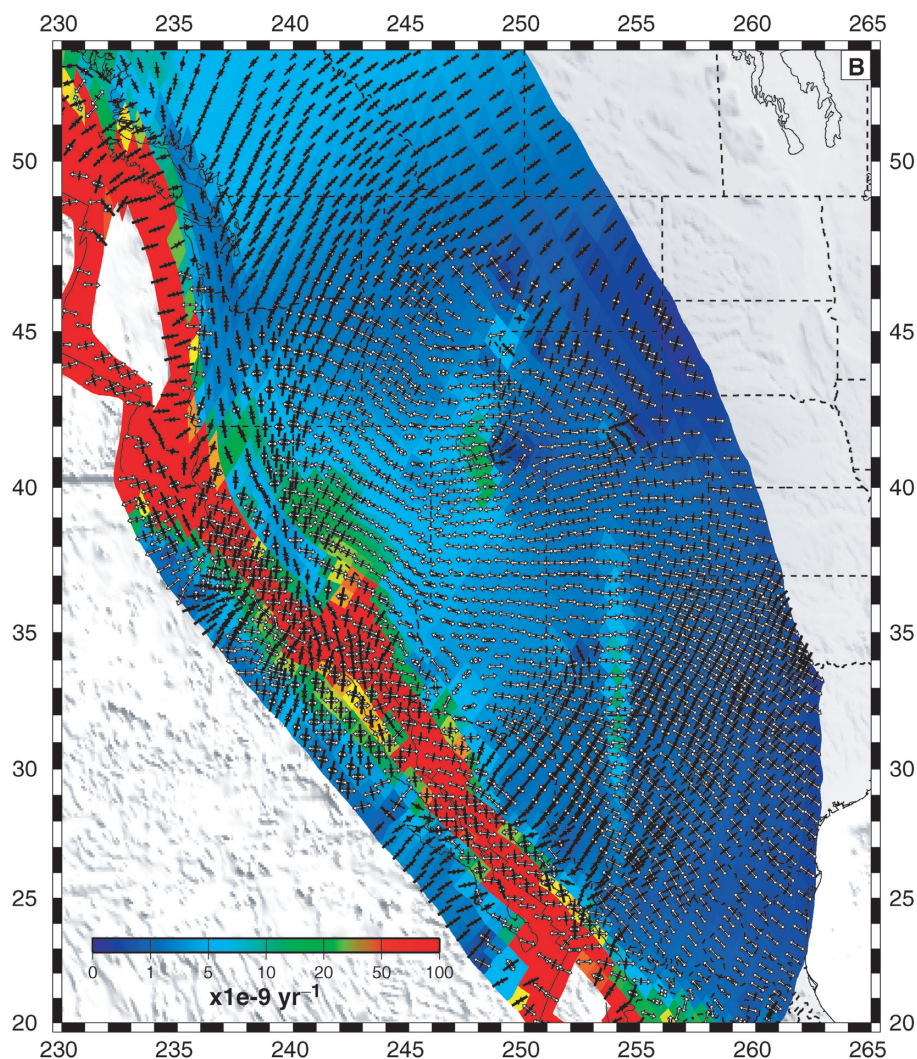


Figure 8. (Continued.)

- plate and estimates of Pacific-North America motion, *Geophys. Res. Lett.*, **22**(24), 3545–3548.
- DeMets, C. & Dixon, T.H., 1999. New kinematic models for Pacific-North America motion from 3 Ma to present, I: Evidence for steady motion and biases in the NUVEL-1A model, *Geophys. Res. Lett.*, **26**(13), 1921–1924.
- DeMets, C. & Stein, S., 1990. Present-day kinematics of the Rivera plate and implications for tectonics in southwestern Mexico, *J. geophys. Res.*, **95**, 21 931–21 948.
- DeMets, C., Gordon, R.G., Argus, D.F. & Stein, S., 1994. Effect of Recent Revisions to the Geomagnetic Reversal Time-Scale On Estimates of Current Plate Motions, *Geophys. Res. Lett.*, **21**(20), 2191–2194.
- Dixon, T.H., Mao, A. & Stein, S., 1996. How rigid is the stable interior of the north American plate?, *Geophys. Res. Lett.*, **23**(21), 3035–3038.
- Dixon, T.H., Miller, M., Farina, F., Wang, H.Z. & Johnson, D., 2000. Present-day motion of the Sierra Nevada block and some tectonic implications for the Basin and Range province, North American Cordillera, *Tectonics*, **19**(1), 1–24.
- England, P. & Houseman, G., 1986. Finite Strain Calculations of Continental Deformation.2. Comparison With the India-Asia Collision Zone, *J. Geophys. Res. Solid Earth Planets*, **91**(B3), 3664–3676.
- England, P. & McKenzie, D., 1982. A Thin Viscous Sheet Model For Continental Deformation, *Geophys. J. R. astr. Soc.*, **70**(2), 295–321.
- Fleitout, L., 1991. The sources of lithospheric tectonic stress, *Phil. Trans. R. Soc. Lond.*, **337**, 73–81.
- Fleitout, L. & Froidevaux, C., 1982. Tectonics and Topography For a Lithosphere Containing Density Heterogeneities, *Tectonics*, **1**(1), 21–56.
- Flesch, L.M., Holt, W.E., Haines, A.J. & Shen-Tu, B.M., 2000. Dynamics of the Pacific-North American plate boundary in the western United States, *Science*, **287**(5454), 834–836.
- Flesch, L.M., Haines, A.J. & Holt, W.E., 2001. Dynamics of the India-Eurasia collision zone, *J. Geophys. Res. Solid Earth*, **106**(B8), 16 435–16 460.
- Frey Mueller, J.T., Murray, M.H., Segall, P. & Castillo, D., 1999. Kinematics of the Pacific North America plate boundary zone, northern California, *J. Geophys. Res. Solid Earth*, **104**(B4), 7419–7441.
- Gan, W.J., Svarc, J.L., Savage, J.C. & Prescott, W.H., 2000. Strain accumulation across the Eastern California Shear Zone at latitude 36 degrees 30'N, *J. Geophys. Res. Solid Earth*, **105**(B7), 16 229–16 236.
- Ghosh, A., Wen, L., Holt, W.E., Haines, A.J. & Flesch, L.M., 2005. Three Dimensional Modeling of Lithosphere and Mantle Dynamics Elucidating Lithosphere-Mantle Coupling, *Eos Trans. AGU*, Fall Meet. Suppl., Abstract U53A–02.
- Ghosh, A., Holt, W.E., Flesch, L.M. & Haines, A.J., 2006. The gravitational potential energy of the Tibetan plateau and the forces driving the Indian plate, *Geology*, **34**(5), 321–324.
- Hammond, W.C. & Thatcher, W., 2005. Northwest basin and range tectonic deformation observed with the global positioning system, 1999–2003, *J. geophys. Res.*, **110**, B10405.
- Haines, A.J. & Holt, W.E., 1993. A Procedure For Obtaining the Complete Horizontal Motions Within Zones of Distributed Deformation From

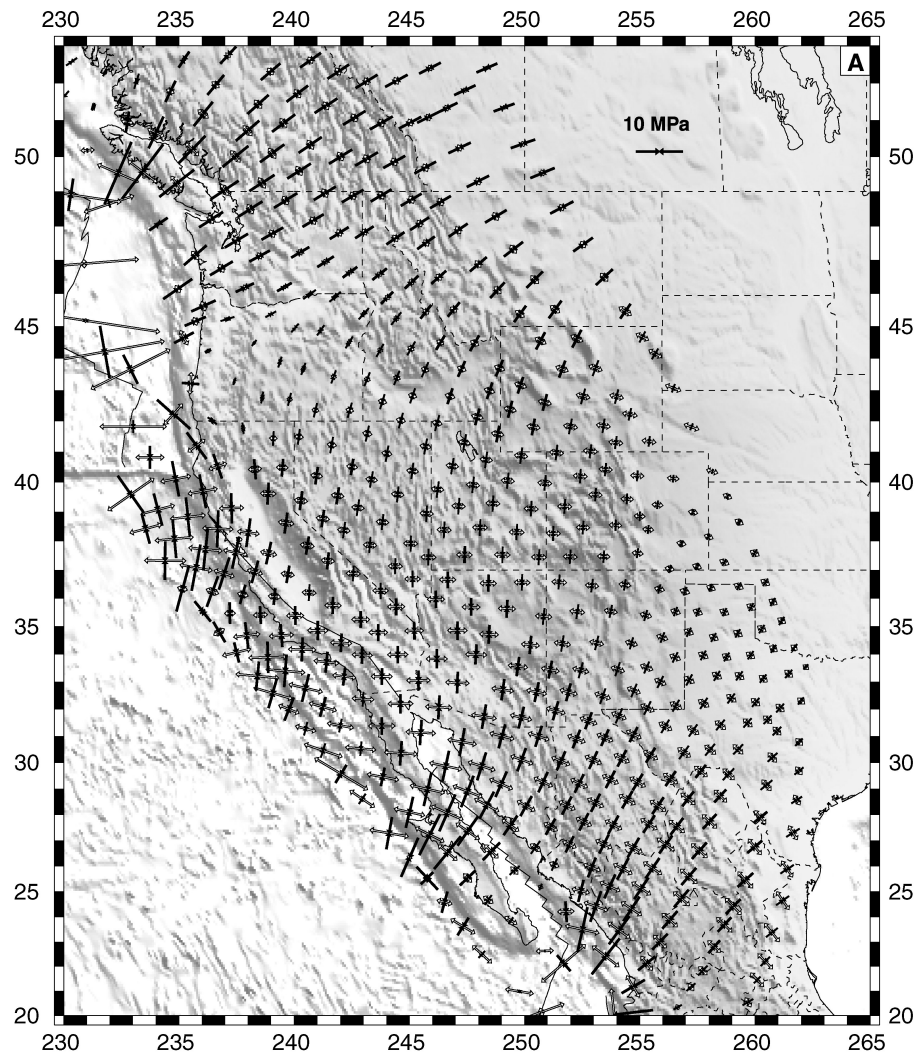


Figure 9. (a) The stress field boundary conditions determined using the long-term strain rate field (Fig. 8b) as stress field indicators and the GPE estimated assuming Airy isostatic balance (Fig. 3a). Open arrows represent tensional principal axes of deviatoric stress, closed arrows compressional principal axes of deviatoric stress. (b) Same as Fig. 9(a) only using the CRUST2.0 data set (Fig. 3b) to determine GPE estimates.

- the Inversion of Strain-Rate Data, *J. Geophys. Res. Solid Earth*, **98**(B7), 12 057–12 082.
- Haines, A.J., Jackson, J.A., Holt, W.E. & Agnew, D.C., 1998. Representing distributed deformation by continuous velocity fields, *Sci. Rep.*, **98**(5), 1–121.
- Haxby, W.F. & Turcotte, D.L., 1978. On isostatic geoid anomalies, *J. geophys. Res.*, **83**(B11), 5473–5478.
- Hetland, E.A. & Hager, B.H., 2004. Relationship of geodetic velocities to velocities in the mantle, *Geophys. Res. Lett.*, **31**, L17604, doi:10.1029/2004GL02069.
- Humphreys, E., Hessler, E., Dueker, K., Farmer, C.L., Ersley, E. & Atwater, T., 2003. How Laramide-age hydration of North American lithosphere by the Farallon slab controlled subsequent activity in the western United States, *Int. Geol. Rev.*, **45**(7), 575–595.
- Jackson, J., 2002. Faulting, flow, and the strength of the continental lithosphere, *Int. Geol. Rev.*, **44**(1), 39–61.
- Jennings, C.W., 1994. Fault Activity Map of California and adjacent areas, California Department of Conservation, Division of Mines and Geology, Sacramento.
- Jones, C.H., Unruh, J.R. & Sonder, L.J., 1996. The role of gravitational potential energy in active deformation in the southwestern United States, *Nature*, **381**(6577), 37–41.
- Kanamori, H. & Anderson, D.L., 1975. Theoretical Basis of Some Empirical Relations in Seismology, *Bull. seism. Soc. Am.*, **65**(5), 1073–1095.
- Khazaradze, G., Qamar, A. & Dragert, H., 1999. Tectonic deformation in western Washington from continuous GPS measurements, *Geophys. Res. Lett.*, **26**(20), 3153–3156.
- Kohlstedt, D.L., Evans, B. & Mackwell, S.J., 1995. Strength of the Lithosphere — Constraints Imposed By Laboratory Experiments, *J. Geophys. Res. Solid Earth*, **100**(B9), 17 587–17 602.
- Kreemer, C., Holt, W.E., Haines, A.J., 2003. An integrated global model of present-day plate motions and plate boundary deformation, *Geophys. J. Int.*, **154**(1), 8–34.
- Lavallee, D. et al., 2001. GPSVEL Project: Towards a Dense Global GPS Velocity Field, *Proceedings of the International Association of Geodesy Scientific Assembly*, Budapest, 2–7 September.
- Lithgow-Bertelloni, C. & Gynn, J.H., 2004. Origin of the lithospheric stress field, *J. geophys. Res.*, **109**, B01408, doi:10.1029/2003JB002467.
- Lowry, A.R., Ribe, N.M. & Smith, R.B., 2000. Dynamic elevation of the Cordillera, western United States, *J. geophys. Res.*, **105**(B10), 23 371–23 390.
- Liu, Z. & Bird, P., 2002. North America plate is driven westward by lower mantle flow, *Geophys. Res. Lett.*, **29**(24), 2164, doi:10.1029/2002GL016002.

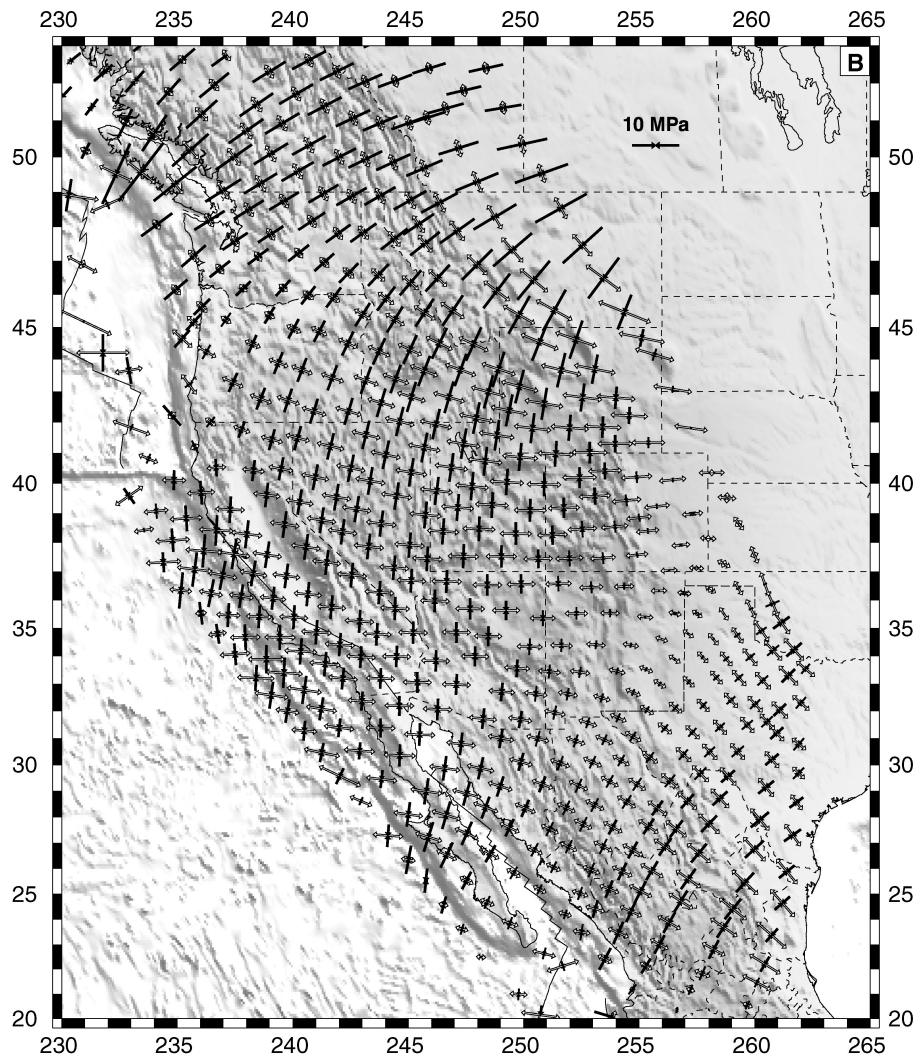


Figure 9. (Continued.)

- Ma, C. & Ryan, J.W., 1998. NASA Space Geodesy Program — GSFC DATA Analysis-1998, VLBI Geodetic Results 1979–1998, August.
- McCaffrey, R., 2005. Block kinematics of the Pacific-North America plate boundary in the southwestern United States from inversion of GPS, seismological, and geologic data, *J. geophys. Res.*, **110**, B07401, doi:10.1029/2004JB003307.
- McCaffrey, R., Long, M.D., Goldfinger, C., Zwick, P.C., Nabelek, J.L., Johnson, C.K. & Smith, C., 2000. Rotation and plate locking at the southern Cascadia subduction zone, *Geophys. Res. Lett.*, **27**(19), 3117–3120.
- McClusky, S.C., Bjornstad, S.C., Hager, B.H., King, R.W., Meade, B.J., Miller, M.M., Monastero, F.C. & Souter, B.J., 2001. Present day kinematics of the Eastern California Shear Zone from a geodetically constrained block model, *Geophys. Res. Lett.*, **28**(17), 3369–3372.
- McKenzie, D.P., 1969. Speculations On Consequences and Causes of Plate Motions, *Geophys. J. R. astr. Soc.*, **18**(1), 1–32.
- Menke, W., 1982. *Geophysical data analysis: Discrete inverse theory*, Academic Press Inc., New York.
- Miller, M.M., Johnson, D.J., Rubin, C.M., Dragert, H., Wang, K., Qamar, A. & Goldfinger, C., 2001a. GPS-determination of along-strike variation in Cascadia margin kinematics: Implications for relative plate motion, subduction zone coupling, and permanent deformation, *Tectonics*, **20**(2), 161–176.
- Miller, M.M., Johnson, D.J., Dixon, T.H. & Dokka, R.K., 2001b. Re-

- finned kinematics of the Eastern California shear zone from GPS observations, 1993–1998, *J. Geophys. Res. Solid Earth*, **106**(B2), 2245–2263.
- Molnar, P., 1992. Mountain Building—Crust in Mantle Overdrive, *Nature*, **358**(6382), 105–106.
- Molnar, P. & Lyon-Caen, H., 1988. Some simple physical aspects of the support, structure, and evolution of mountain belts, *Spec. Pap. Geol. Soc. Am.*, **218**, 179–207.
- Montesi, L.G.J., 2004. Controls of shear zone rheology and tectonic loading on postseismic creep, *J. geophys. Res.*, **109**(B10), B10404.
- Mooney, W.D., Laske, G. & Masters, T.G., 1998. CRUST 5.1: A global crustal model at 5 degrees x 5 degrees, *J. Geophys. Res. Solid Earth*, **103**(B1), 727–747.
- Morse, P.M. & Feshbach, H., 1953. *Methods of Theoretical Physics*, pp. 257–347, McGraw-Hill, New York.
- Oldow, J.S., 2003. Active transtensional boundary zone between the western Great Basin and Sierra Nevada block, western US cordillera, *Geology*, **31**(12), 1033–1036.
- Panasjuk, S.B. & Hager, B.H., 2000. Models of isostatic and dynamic topography, geoid anomalies, and their uncertainties, *J. geophys. Res.*, **105**(B12), 28 199–28 209.
- Petersen, M.D. & Wesnousky, S.G., 1994. Fault Slip Rates and Earthquake Histories For Active Faults in Southern California, *Bull. seism. Soc. Am.*, **84**(5), 1608–1649.

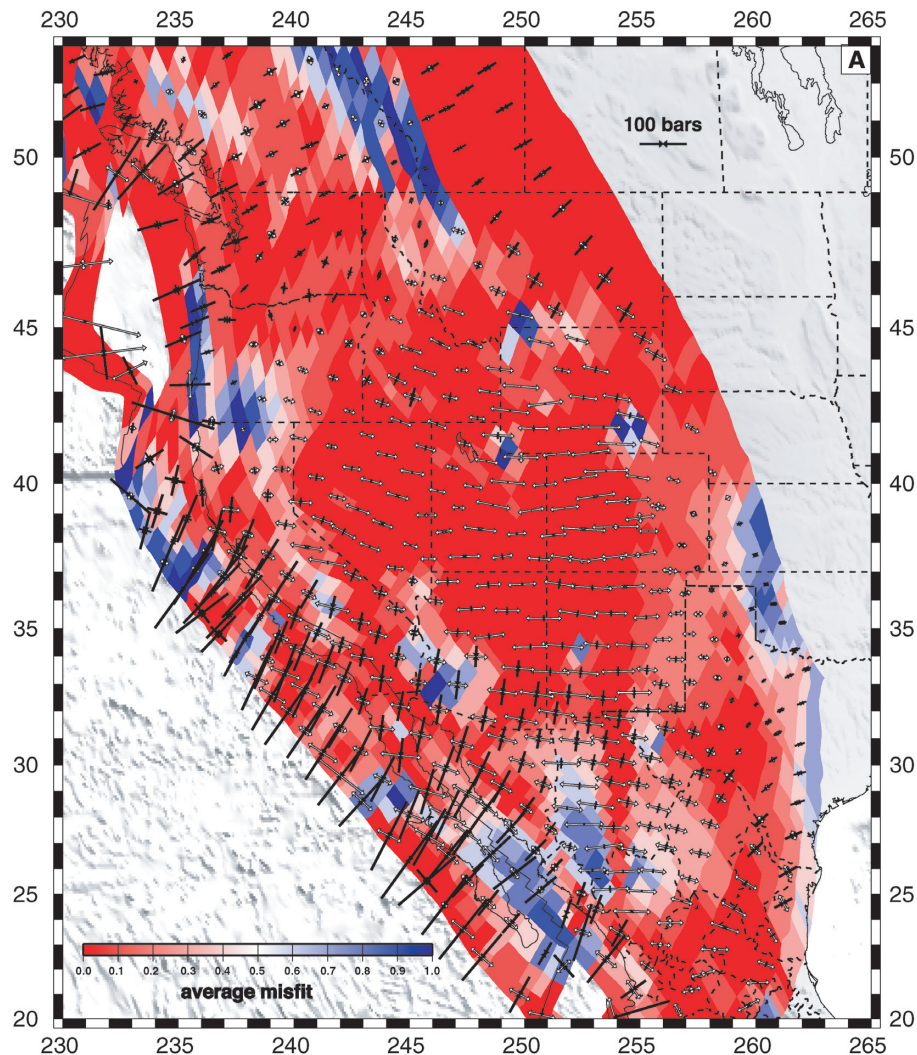


Figure 10. (a) The long-term total deviatoric stress field determined from GPE estimates that assume Airy isostatic balance plus boundary conditions in Fig. 9(a). Open arrows represent tensional principal axes of deviatoric stress, closed arrows compressional principal axes of deviatoric stress. The misfit function (eq. 21) between deviatoric stress and the strain rate is plotted in the background (see also Table 1 for misfit results by region). (b) Same as Fig. 10(a) only using the CRUST2.0 data set to determine GPE estimates and boundary conditions in 9(b).

Plafker, G. & Berg, H.C., 1994. Overview of the geology and tectonic evolution of Alaska, in *The Geology of North America*, series v. G-1, pp. 989–1021, eds Plafker, G. & Berg, H.C., GSA, Boulder, CO.

Pollitz, F.F., 2003. The relationship between the instantaneous velocity field and the rate of moment release in the lithosphere, *Geophys. J. Int.*, **153**, 596–608.

Pollitz, F.F., Burgmann, R. & Segall, P., 1998. Joint estimation of afterslip rate and postseismic relaxation following the 1989 Loma Prieta earthquake, *J. geophys. Res.*, **103**(11), 26 975–26 992.

Prescott, W.H., Savage, J.C., Svarc, J.L. & Manaker, D., 2001. Deformation across the Pacific-North America plate boundary near San Francisco, California, *J. geophys. Res.*, **106**(B4), 6673–6682.

Richardson, R.M., 1987. Modeling the tectonics of the Indo-Australian plate (abstract), *Eos Trans. AGU*, **68**, 1466.

Richardson, R.M. & Coblenz, D., 1994. Stress modeling in the Andes: Constraints on the South American intralate stress magnitudes, *J. Geophys. Res.*, **99**, 22 015–22 025.

Richardson, R.M. & Reding, L.M., 1991. North American plate dynamics, *J. geophys. Res.*, **96**, 12 201–12 223.

Savage, J.C., Gan, W., Prescott, W.H., Svarc, J.L., 2004. Strain accumulation across the Coast Ranges at the latitude of San Francisco, 1994–2000, *J. geophys. Res.*, **109**(B3): Art. No. B03413.

Sauber, J., McClusky, S. & King, R., 1997. Relation of ongoing deformation rates to the subduction zone process in southern Alaska, *Geophys. Res. Lett.*, **24**(22), 2853–2856.

Shen-Tu, B., Holt, W.E. & Haines, A.J., 1998. Contemporary kinematics of the western United States determined from earthquake moment tensors, very long baseline interferometry, and GBS observations, *J. Geophys. Res. Solid Earth*, **103**(B8), 18 087–18 117.

Shen-Tu, B.M., Holt, W.E. & Haines, A.J., 1999. Deformation kinematics in the western United States determined from Quaternary fault slip rates and recent geodetic data, *J. Geophys. Res. Solid Earth*, **104**(B12), 28 927–28 955.

Sibson, R.H., 1982. Fault Zone Models, Heat-Flow, and the Depth Distribution of Earthquakes in the Continental-Crust of the United-States, *Bull. seism. Soc. Am.*, **72**(1), 151–163.

Silver, P.G. & Holt, W.E., 2002. The mantle flow field beneath western North America, *Science*, **295**, 1054–1057.

Sonder, L.J. & Jones, C.H., 1999. Western United States extension: How the West was widened, *Ann. Rev. Earth planet. Sci.*, **27**, 417–466.

Steinberger, B. & OConnell, R.J., 1998. Advection of Plumes in mantle flow: implication for hotspot motion, mantle viscosity and plume distribution, *Geophys. J. Int.*, **132**(2), 412–434.

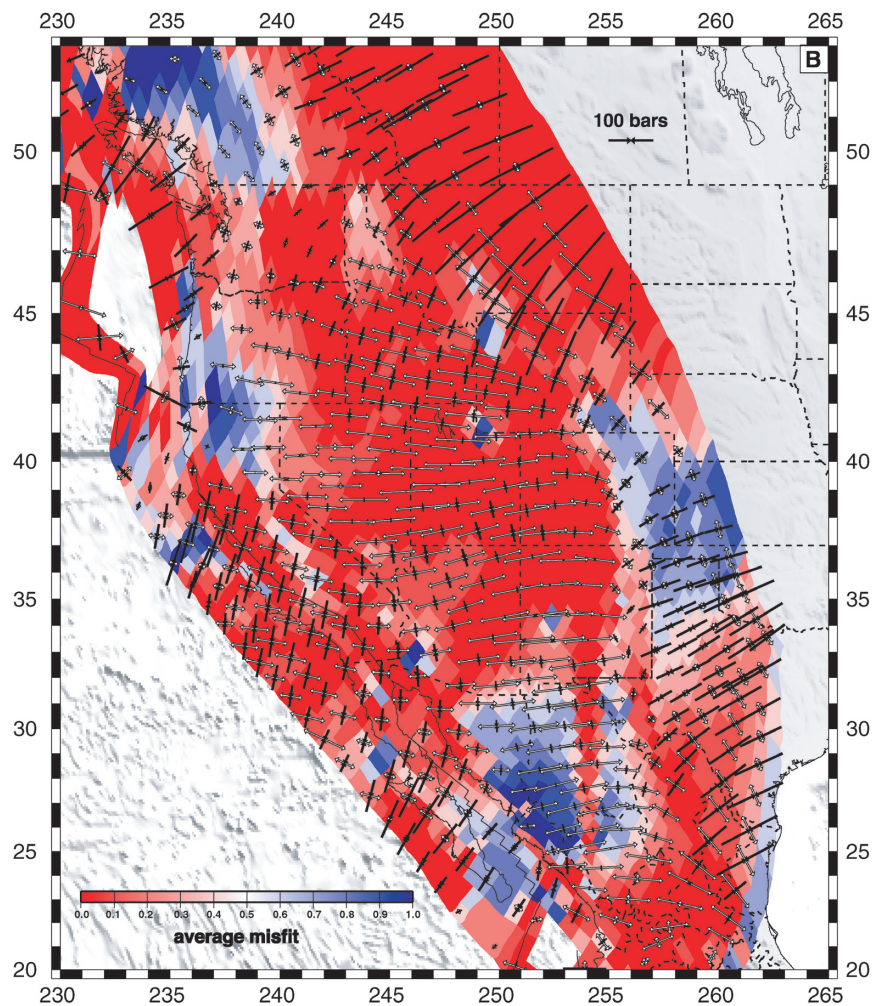


Figure 10. (Continued.)

- Stock, J. & Molnar, P., 1988. Uncertainties and Implications of the Late Cretaceous and Tertiary Position of North-America Relative to the Farallon, Kula, and Pacific Plates, *Tectonics*, **7**(6), 1339–1384.
- Su, W.J., Woodward, R.L. & Dziewonski, A.M., 1994. Degree-12 model of shear velocity heterogeneity in the mantle, *J. geophys. Res.*, **99**, 6945–6980.
- Svarc, J.L., Savage, J.C., Prescott, W.E. & Murray, M.H., 2002a. Strain accumulation and rotation in western Oregon and southwestern Washington, *J. geophys. Res.*, **107**(B5), Art. No. 2087.
- Svarc, J.L., Savage, J.C., Prescott, W.H. & A.R. Ramelli, 2002b. Strain accumulation and rotation in western Nevada, 1993–2000, *J. geophys. Res.*, **107**(B5), Art. No. 2090.
- Thatcher, W., 2003. GPS constraints on the kinematics of continental deformation, *Int. Geol. Rev.*, **45**(3), 191–212.
- Tovish, A., Schubert, G. & Luyendyk, B.P., 1978. Mantle Flow Pressure and the Angle of Subduction – Non-Newtonian Corner Flows, *J. geophys. Res.*, **83**(B12), 5892–5898.
- Townend, J. & Zoback, M.D., 2004. Regional tectonic stress near the San Andreas fault in central and southern California, *Geophys. Res. Lett.*, **31**(15), L15S11.
- Townsend, D.A. & Sonder, L.J., 2001. Rheologic control of buoyancy-driven extension of the Rio Grande rift, *J. geophys. Res.*, **106**(B8), 16 515–16 523.
- Wdowinski, S. & O’connell, R.J., 1991. Deformation of the Central Andes (15-Degrees-S-27-Degrees-S) derived from a flow model of subduction zones, *J. Geophys. Res. Solid Earth Planets*, **96**(B7), 12 245–12 255.
- Wells, R.E., Weaver, C.S., Blakely, R.J., 1998. Fore-arc migration in Cascadia and its neotectonic significance, *Geology*, **26**(8), 759–762.
- Wen, L. & Anderson, D.L., 1995. The fate of slabs inferred from seismic tomography and 130 million of subduction, *Earth planet. Sci. Lett.*, **133**, 185–198.
- Wen, L. & Anderson, D.L., 1997a. Layered mantle convection: a model for geoid and topography, *Earth planet. Sci. Lett.*, **146**(3–4), 367–377.
- Wen, L. & Anderson, D.L., 1997b. Slabs, hotspots, cratons and mantle convection revealed from residual tomography in the upper mantle, *Phys. Earth planet. Int.*, **99**, 131–143.
- Wen, L. & Anderson, D.L., 1997c. Present-day plate motion constraint on mantle rheology and convection, *J. geophys. Res.*, **102**, 24 639–24 653.
- Wilson, D.S., 1993. Confidence-intervals for motion and deformation of the Juan-de-Fuca plate, *J. geophys. Res.*, **98**, 16 053–16 071.
- Whitehouse, P.L., England, P.C. & Houseman, G.A., 2005. A physical model for the motion of the Sierra Block relative to North America, *Earth planet. Sci. Lett.*, **237**(3–4), 590–600.
- Zhong, S. & Gurnis, M., 1996. Interaction of weak faults and non-Newtonian rheology produces plate tectonics in a 3D model of mantle flow, *Nature*, **383**(6597), 245–247.
- Zoback, M.D. & Zoback, M.L., 1991. Tectonic stress field of North America and relative plate motions, *Neotectonics of North America*, pp. 339–366, eds Slemmons, D.B., Engdahl, E.R., Zoback, M.D. & Blackwell, D.D., Boulder, CO.
- Zoback, M.L., 1989. State of Stress and Modern Deformation of the Northern Basin and Range Province, *J. geophys. Res.*, **94**(B6), 7105–7128.
- Zoback, M.L. & Mooney, W.D., 2003. Lithospheric buoyancy and continental intraplate stress, *Int. Geology Rev.*, **45**(2), 95–118.
- Zoback, M.L. & Zoback, M., 1980. State of Stress in the Conterminous United-States, *J. geophys. Res.*, **85**(B11), 6113–6156.

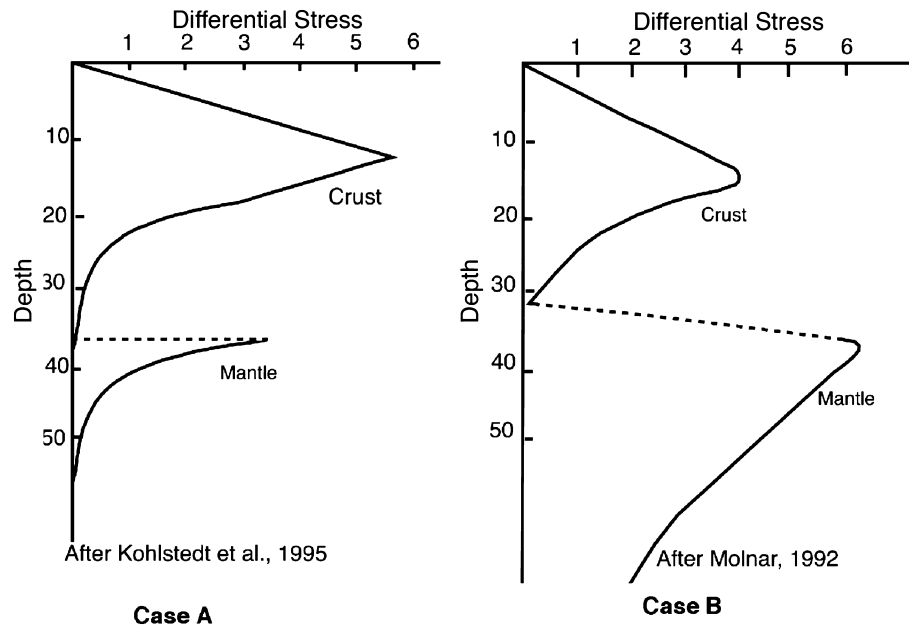


Figure 11. The two end-member strength profiles used in Section 4 to investigate the vertical distribution of stress in the lithosphere. Note that the exact strength magnitudes on the horizontal axis are not important in the above calculations, only the shape of the strength profile. What is important is the integral under the strength profile, which must equal the magnitude of the vertically averaged deviatoric stress calculated in Section 3 (Figs 5 and 10).

APPENDIX A:

The vertical stress in eq. (6) is

$$\sigma_{zz}(z) = - \int_{-h}^z \rho(z')g dz', \tag{A1}$$

where ρ is the density, g is acceleration of gravity. Taking the vertical average of eq. (A1) the vertically averaged vertical stress is expressed as:

$$\bar{\sigma}_{zz} = - \frac{1}{L} \int_{-h}^L \left[\int_{-h}^z \rho(z')g dz' \right] dz. \tag{A2}$$

Again eq. (A2) is defined to be referenced to the base of the lithosphere that is at uniform depth $z = L$. Expanding eq. (A2) yields

$$\bar{\sigma}_{zz} = - \frac{1}{L} \int_{-h}^L (L - z') \rho(z')g dz'. \tag{A3}$$

The isostatic geoid is proportional to a constant given by

$$N \propto \int_0^L \rho(z')z'g dz' = L\bar{\sigma}_{zz} - \int_{-h}^0 \rho(z')z'g dz' + L \int_{-h}^L \rho(z')g dz', \tag{A4}$$

where N is the geoid anomaly (Haxby & Turcotte 1978), and the last integral on the right-hand side of (A4) is constant in the case of isostatic equilibrium. The left-most integral from 0 to L in eq. (A4) is commonly used, incorrectly, to define gravity potential energy. However, eq. (A4) can be substituted approximately correctly for GPE for the purpose of stress field calculations if the lithosphere is isostatically compensated, because in such a case the constant in (A4) makes no contribution to the deviatoric stress field. Moreover, (A4) is valid for the geoid only when isostatic balance applies anyway. In addition, the reference level for eq. (A4) is the surface, not the base of the lithosphere, as it should be for depth integrals in thin sheet calculations. Thus, eq. (A4) can only be used if there is no dynamic topography (topography is completely compensated by either the Pratt or Airy mechanism within the lithospheric lid). Since there is dynamic topography in the western US (Lowry *et al.* 2000; Panasyuk & Hager 2000), the geoid should be used with caution as a proxy for GPE differences there. Cases where (A4) will suffice as a proxy for the estimate of GPE differences is where the last integral in (A4) varies only over long-wavelengths and on short wavelengths it approximates a constant.

SUPPLEMENTARY MATERIAL

The following supplementary material is available for this article:

Appendix S1. A series of supplementary Figs S1a to S3l, and supplementary Table S1.

This material is available as part of the online article from: <http://www.blackwell-synergy.com/doi/abs/10.1111/j.1365-246X.2007.03274.x>
(This link will take you to the article abstract).

Please note: Blackwell Publishing are not responsible for the content or functionality of any supplementary materials supplied by the authors. Any queries (other than missing material) should be directed to the corresponding author for the article.